
GAZİ ÜNİVERSİTESİ
Gazi
1926

NUMERICAL INVESTIGATION OF AERODYNAMIC PERFORMANCE OF VERTICAL AXIS WIND TURBINE

A THESIS SUBMITTED TO
THE GRADUATE SCHOOL OF NATURAL AND APPLIED SCIENCES
OF
GAZİ UNIVERSITY

BY

Sinem KESKİN

IN PARTIAL FULFILLMENT OF THE REQUIREMENTS
FOR
THE DEGREE OF MASTER OF SCIENCE
IN
DEPARTMENT OF ENERGY SYSTEMS ENGINEERING

JULY 2023

ETHICAL STATEMENT

I hereby declare that in this thesis study I prepared in accordance with the thesis writing rules of Gazi University Graduate School of Natural and Applied Sciences;

- All data, information and documents presented in this thesis have been obtained within the scope of academic rules and ethical conduct,
- All information, documents, assessments and results have been presented in accordance with scientific ethical conduct and moral rules,
- All material used in this thesis that are not original to this work have been fully cited and referenced,
- No change has been made in the data used,
- The work presented in this thesis is original,

or else, I admit all loss of rights to be incurred against me.

Sinem KESKİN

28/07/2023

NUMERICAL INVESTIGATION OF AERODYNAMIC PERFORMANCE OF VERTICAL AXIS WIND TURBINE

(M. Sc. Thesis)

Sinem KEKSİN

GAZİ UNIVERSITY

GRADUATE SCHOOL OF NATURAL AND APPLIED SCIENCES

July 2023

ABSTRACT

In this thesis study, a virtual roughness element was employed on the blades of a H-type Darrieus vertical axis wind turbine (VAWT) with NACA 0018 blades and its effect on turbine performance was investigated. The optimum length of the roughness device and its location on the blade are presented with 2D analyses. The roughness heights depending on the chord length were investigated as k/c: 0.003, 0.006, 0.009, 0.012 and chordwise roughness ratios on the surface are 5%, 10%, and 50%. Time-dependent torque changes were obtained via ANSYS Fluent 18.2 software, therefore the variation of power coefficient over time was evaluated taking into consideration tip speed ratio. The results of the x velocity component and turbulence kinetic energy distributions in different x/c and k/c dimensionless parameters were compared in terms of examining their effects on turbine aerodynamics. Numerical results showed that the best power coefficient values were achieved at the chordwise roughness ratio on the surface: 50% (x/c: 0-0.50). Since the highest efficiency was achieved at this x/c: 0-0.50 value, this x/c range was highlighted in terms of roughness height. As the roughness ratios k/c: 0.003, 0.006, 0.009, and 0.012 were analyzed, the maximum power coefficient was obtained at k/c: 0.012. In addition, in the case where the x/c: 0 – 0.50 location was applied to the roughness element, the power coefficient improved with increasing roughness height. Thus, it has been observed that the roughness element, which is a passive control technique, contributes to the aerodynamic performance of the turbine by reducing the flow separations in VAWTs.

Science Code	:	92806
Key Words	:	Vertical axis wind turbine, power coefficient, aerodynamic performance.
Page Number	:	49
Supervisor	:	Prof. Dr. Mustafa İLBAŞ
Co-Supervisor	:	Prof. Dr. Mustafa Serdar GENÇ

DİKEY EKSENLİ RÜZGAR TÜRBİNİNİN AERODİNAMİK PERFORMANSININ SAYISAL İNCELENMESİ

(Yüksek Lisans Tezi)

Sinem KESKİN

GAZİ ÜNİVERSİTESİ

FEN BİLİMLERİ ENSTİTÜSÜ

Temmuz 2023

ÖZET

Bu tez çalışmasında, NACA 0018 kanadına sahip H-tipi Darrieus dikey eksenli rüzgâr türbininin (DERT) kanatlarında sanal bir pürüzlülük elemanı kullanılmış ve bunun türbin performansı üzerindeki etkisi incelenmiştir. Pürüzlülük elemanının optimum uzunluğu ve kanat üzerindeki konumu iki boyutlu analizlerle sunulmuştur. Kiriş uzunluğuna bağlı pürüzlülük yükseklikleri k/c: 0.003, 0.006, 0.009, 0.012 olarak ve yüzeydeki veter uzunluğuna bağlı pürüzlülük oranları %5, %10, %50 olarak incelenmiştir. Zamana bağlı tork değişimleri, ANSYS Fluent 18.2 yazılımı aracılığıyla elde edilmiştir, bu sayede güç katsayısının zamana göre değişimi, uç hız oranı dikkate alınarak değerlendirilmiştir. X hız bileşeni ve türbülans kinetik enerji dağılımlarının farklı x/c ve k/c boyutsuz parametrelerdeki sonuçları türbin aerodinamiği üzerindeki etkilerinin incelenmesi açısından karşılaştırılmıştır. Sayısal sonuçlar, en iyi güç katsayısı değerlerinin yüzeyde veter uzunluğuna bağlı pürüzlülük oranı %50 (x/c: 0-0.50) olduğunda elde edildiğini göstermiştir. En yüksek verim bu x/c: 0-0.50 değerinde elde edildiğinden pürüzlülük yüksekliği açısından bu x/c aralığı ön plana çıkarılmıştır. Pürüzlülük oranları k/c: 0.003, 0.006, 0.009 ve 0.012 incelendiğinde k/c: 0.012'de maksimum güç katsayısı elde edilmiştir. Ayrıca pürüzlülük elemanının x/c: 0 – 0.50 konumuna uygulandığı durumda, artan pürüzlülük yüksekliği ile güç katsayısı iyileşmiştir. Böylece pasif bir kontrol tekniği olan pürüzlülük elemanının DERT'lerdeki akış ayrımlarını azaltarak türbinin aerodinamik performansına katkı sağladığı gözlemlenmiştir.

Bilim Kodu	:	92806
Anahtar Kelimeler	:	Dikey eksenli rüzgâr türbini, güç katsayısı, aerodinamik performans.
Sayfa Adedi	:	49
Danışman	:	Prof. Dr. Mustafa İLBAŞ
İkinci Danışman	:	Prof. Dr. Mustafa Serdar GENÇ

ACKNOWLEDGEMENTS

I would like to express my sincere thanks to my advisor, Prof. Dr. Mustafa İLBAŞ, and co-supervisor, Prof. Dr. Mustafa Serdar GENÇ, for their support and tolerance in every process of my thesis study. I would like to thank Assoc. Prof. Dr. İlyas KARASU and Anıl Eren SEZER, conveyed their knowledge about ANSYS Fluent software to me and helped me with all my questions and Assoc. Prof. Dr. Serhat KARYEYEN for attentively reviewing my study and providing suggestions. I would like to express my gratitude to my dear mother Semra KESKİN, my father İlhan KESKİN and my brother Sezer KESKİN, who have always supported me throughout my life, to my dear friends Özkan Mert ÖZTÜRK, Belemir GÜRDAL and Funda İHTİYAR who have been a source of motivation for me during my thesis process and in my education life.

I would like to thank TÜBİTAK for financially supporting this thesis within the scope of the 2210-D Industrial Graduate Scholarship Program.

TABLE OF CONTENTS

Page

LIST OF TABLES

Table **Page**

LIST OF FIGURES

Figure **Page**

Figure **Page**

SYMBOLS AND ABBREVIATIONS

Symbols and abbreviations used in this study are presented below with their explanations.

Symbols	Explanations
C	Blade chord
C_D	Drag coefficient
C_L	Lift coefficient
C_N	Normal force coefficient
C_P	Power coefficient
C_T	Tangential force coefficient
C_Q	Torque coefficient
D	Rotor diameter
k	Roughness height
N	Number of blade
R	Rotor radius
Re	Reynolds number
U_∞	Freestream wind speed
Vt	Tangential velocity
Vn	Normal velocity
W	Relative velocity
δ	Boundary layer thickness
ρ	Air density
μ	Dynamic viscosity
ω	Angular velocity
λ	Tip speed ratio
θ	Azimuthal angle
α	Angle of attack
x	Streamwise direction

Abbreviations	Explanations
AoA	Angle of attack
CFD	Computational fluid dynamics
HAWT	Horizontal axis wind turbine
LSB	Laminar separation bubble
NACA	National Advisory Committee for Aeronautics
RANS	Reynolds-Averaged Navier-Stokes
TSR	Tip speed ratio
VAWT	Vertical axis wind turbine

1. INTRODUCTION

The requisition for renewable energy sources has enhanced dramatically as a consequence of the scarcity of fossil fuels and the increment in the releases of greenhouse gases. Novel renewable alternative energy has become crucial to ensure the progress of a sustainable and reliable economy. Particularly, wind power has become a competitive alternative to conventional fossil fuel-based energy sources. The wind is the most advanced and potential energy provider within renewable energy sources owing to its clean and limitless qualities. The essential approach to harnessing wind energy is the operation of transforming the kinetic energy of the wind into electricity through a wind turbine. Wind turbines have been identified as horizontal axis wind turbines (HAWTs) and vertical axis wind turbines (VAWTs) based on the rotating axis of blades by the direction of the wind flow.

A wind turbine classified as HAWT includes a main rotor shaft and blades that rotate on a horizontal axis. It is the most typical and extensively applied design for producing vast amounts of wind energy and these turbines are frequently dispersed throughout vast wind farms. Wind flows across the blades as it blows, producing lift forces similar to those on an airplane wing. The blades rotate around the hub as a result of this lift force. The main rotor shaft transmits the rotation to the gearbox, which speeds up the rotation and transfers the energy to the generator. The minimum wind speed below which the turbine commences to yield utilizable electrical output is recognized as the cut-in wind speed. This usually occurs at a speed of 3 to 4 meters per second (m/s). The turbine may not generate sufficient power below this speed. The wind speed that is achieved when the turbine produces its highest-rated power output is recognized as the rated wind speed. Although it might change, this speed is frequently between 12 and 15 m/s. The cut-out wind speed is the highest wind speed that occurs when a turbine must be shut down to avoid damage. Depending on the design, it is often between 25 and 30 m/s or higher. HAWTs have large power sway and yaw mechanism, and complicated design formation.

VAWTs are a form of wind turbine in which the primary rotor shaft is situated vertically, as opposed to HAWTs where the rotor axis is horizontal. There are numerous variations in the designs and configurations of VAWTs. To begin producing electricity, VAWTs need wind speeds of at least 3-4 m/s. Depending on the specific design, the optimum velocity range for

obtaining maximum power varies, although it generally lies between 12 and 25 m/s. For to protect the system, VAWTs may shut down or enter a safety mode whenever they exceed a predetermined speed limit, often 25 to 30 m/s. VAWTs can easily operate in wind conditions with turbulence, including gusts and turbulence near structures or obstructions.

As compared with HAWTs, VAWTs provide a variety of benefits which includes reduced noise levels, simplified maintenance, and improved performance in turbulent wind flow. VAWTs are a desirable option for small-scale wind power generation because of these benefits, particularly in urban environments where space is at a premium and wind direction and speed are unpredictable. A detailed examination of the concepts reveals that VAWTs are appropriate for generating energy in situations when typical HAWTs lack the capability of providing adequate operational effectiveness, especially in extreme wind speeds and turbulent wind flows. The fact that VAWTs are omnidirectional without any inherent insensitivity to wind direction. They also accept wind from all directions without a yawing device is another significant benefit. These lead to VAWTs suitable for urban areas and, in general, environments with skewed and unsteady wind characteristics [1-6].

However, VAWT designs still tend to have complex rotor aerodynamics caused by a continually varying angle of attack (AoA) and indigent self-starting attitudes, which generally results in reduced efficiency and a higher cost per unit of produced energy. The application areas and spreading of the VAWTs have been restricted by these drawbacks [7]. Various methods, including modifying operating aerodynamic characteristics and designing specialized airfoil profiles for VAWTs and small-scale unmanned aerial air vehicles, are being investigated to enhance aerodynamic performance [8-18].

Since systems such as wind turbines and micro-aerial vehicles are small and move at low speeds, utilizing additional performance-enhancing equipment is exceedingly burdensome and high-priced. In addition, movement or flight can be achieved by overcoming the system weights in the above-mentioned air vehicles. This also occurs at low speeds; the wind turbine can operate at 3 to 4 m/s of wind speed, and the micro-aircraft can obtain a lifting force from its weight by spending considerable amounts of fuel. The existence of the aforementioned problems and the inadequateness of the current solutions necessitate advancements in the relevant technical area. With the view to struggling with these concerns, passive flow control systems are required to minimize early separation caused by the effect of viscous forces on

the blade structures of small-sized wind turbines working at low Reynolds numbers and to enhance the power generation of the turbines. Active and passive control systems are two different approaches used to increase performance and ensure safe operation, preventing the occurrence of laminar separation bubble (LSB) on wind turbine blades.

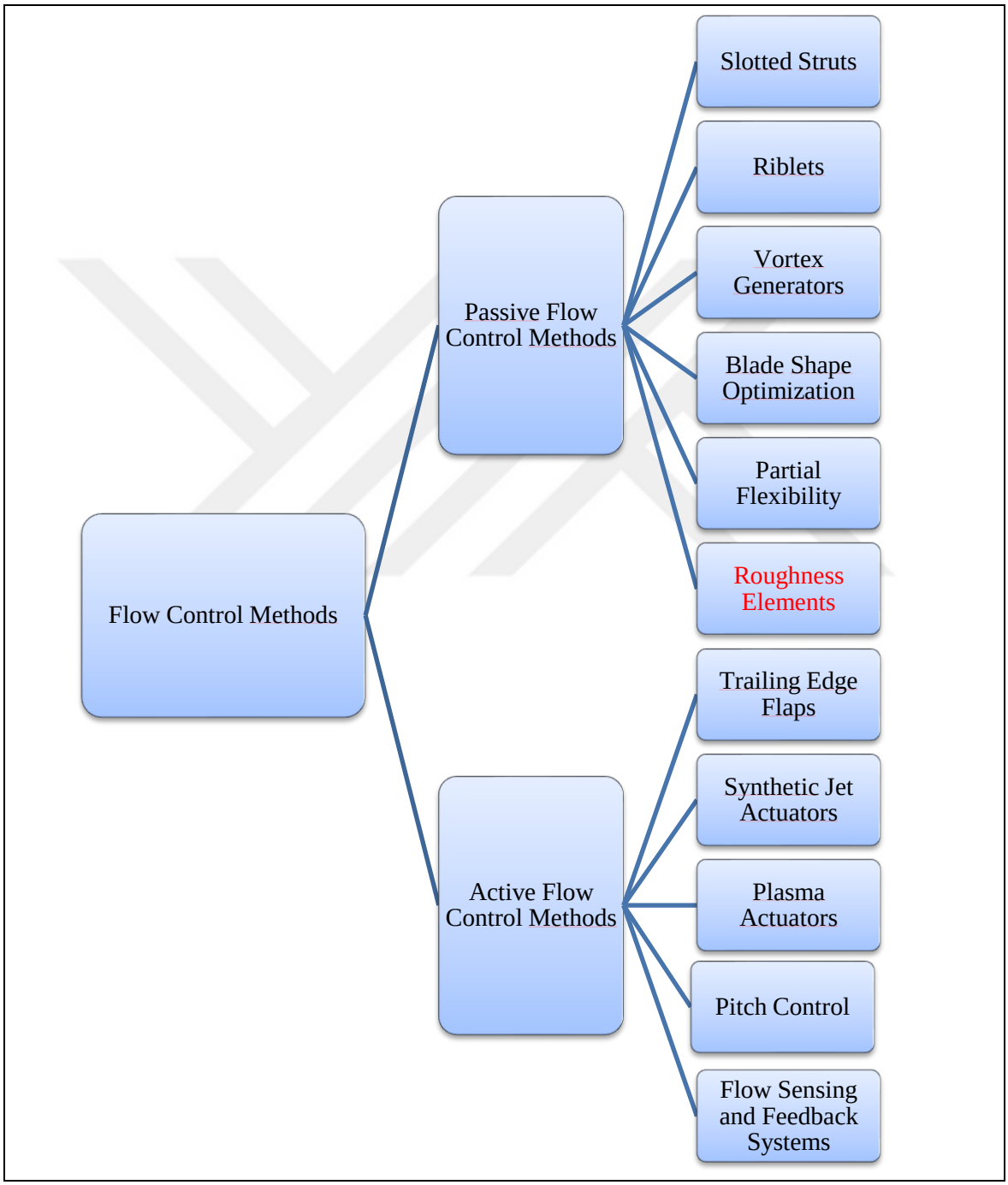

Figure 1.1. Different flow control techniques

An important general structure for a VAWT is the strut, which is also known as the support component. The struts, which are used in both spiral and straight blade VAWTs, offer structural rigidity to withstand loads to which the blade is subjected (aerodynamic, gravitational, and inertial), as well as in charge of conveying torque to the shaft to provide energy output and have a significant impact on the rotor's inherent frequency [19]. Riblets are grooves carved into the surface of the flow pattern; a sort of covering influenced by the moving ability of the shark. These small channels throughout the flow control the flow and diminish the cross-velocity component within the channels, which reduces friction [20]. The basic concept underlying vortex generators is rather straightforward: by moving fluid with significant momentum value near the surface, they produce vortex motions that stimulate the boundary layer on the targeted blade surface to which they ensure flow attachment, leading to improved aerodynamic performance [21,22]. The effects of partial flexibility as a passive control method on suction and pressure surfaces were examined, including flow phenomena over various wind turbine blades at varying AoA [23-25].

The wind turbine aerodynamics scientists preferred the flaps to augment aerodynamic performance, in addition, to load alleviation and reducing vortex-induced vibration [22,26,27]. It is possible to control the separated flow and vortex-related structure precisely and successfully in complex unstable flow utilizing the active flow control technique known as plasma [28-30]. The blade pitch angle control system might be used for VAWTs t to access the profitability of the pitch control system and raise the moment coefficient of VAWTs [31].

The use of roughness elements as a passive control method has been a controversial issue because it can have either a favourable or detrimental effect on the turbine power coefficient according to the position and length of the roughness devices. In this context, the effect of roughness application on LSB at pre-stall and post-stall conditions for low Reynolds number flows has been examined in different airfoils. The purpose of this thesis is to determine the location and chordwise length of the roughness elements on the blade’s upper surface that trigger the transition to turbulence and accelerate the transition to bypass turbulence, as well as the effect of local roughness on the aerodynamic performance of the blade configurations of VAWTs used in the energy sector. At the roughness location with the optimum value, turbine torque and mechanical efficiency were examined numerically. For the first time in the literature, this method will be numerically tested on vertical axis turbine blades with the

help of academic-based ANSYS Fluent software, determining turbine performance at a certain TSR value. In this thesis, the performance of a model VAWT is considered numerically, employing roughness element on the blade's surface and detailed information about the length of the roughness application and its location on the blade is presented.

2. LITERATURE REVIEW

In recent decades, studies on the design parameters, performance evaluations, and flow controls of vertical axis turbines have increased due to their adaptability to offshore and urban applications. However, these turbines suffer from a lack of experimental data to validate in terms of numerical modeling in many conditions. After a detailed glance at the literature, there has been relatively limited research on how the utilization of roughness elements on VAWT airfoils affects performance and flow phenomena over the blades.

An exhaustive assessment of a great deal of VAWT blades with numerous types is performed to determine an appropriate type design for VAWT by Miao et al [32]. As the aerodynamic efficiency, the effect of bale tip loss, and the start-up performance of VAWT are analyzed, it was revealed that the redesigned winglet reduced tip degradation in the upwind zone and hindered flow separation in the downwind zone at the optimum tip speed ratio, considerably enhancing its outcomes in one rotor cycle. Ma et al. suggested an automated air profile optimizing approach that includes the paramedic model and calculation phases owing to contributing to the power performance of the high-solidity VAWT. The optimization system introduced parameters to create and validate a reliable numerical simulation of a three-bladed VAWT at different TSRs. The power performance of the VAWT has undergone significant enhancements by optimizing the blades. The highest power coefficient growth rate takes place at TSR=0.9, taking advantage of the augmentation in torque value in the azimuth angle range [33].

The performance of a micro VAWT with variable pitch is scrutinized, performing both experimental and numerical methods by M. Elkhoury et al [34]. The numerical simulations in three dimensions are used since the VAWT uses three straight blades with a low aspect ratio (AR). In order to associate flow structure, a large eddy simulation based on the dynamic Smagorinsky subgrid-scale model is operated, while the performance of the VAWT was examined with wind tunnel measurements. Both experimentally and numerically, the influence of wind velocity, turbulence intensity, airfoil design, and support structure with baseline and variable-pitch cases were considered based on the performance of the wind turbine, and this alteration was extensively evaluated. Tescione et al. [35] conducted experimental studies for the progress of the near wake of the VAWT, conducting PIV

measurement techniques. The experiments were carried out using an H-type rotor with a TSR = 4.5 and at Re = 1.7 x 10^5. The results demonstrate the development of the vorticity shed by the blade, the formation of large quantities of vortex formations, the edges of the wake and the structure of an unsymmetrical induction region in the wake. Vergaerde et al. [36] carried out three-dimensional velocity measurements in the wake region to examine the power increase of two VAWTs positioned side by side. It was shown that the rotational directions of paired VAWTs cause different wakes. The isolated and three counter-rotating configurations were compared in terms of length, width, and replenishment. Santamaria et al. [37] considered a novel approach for the performance analysis of small-scale VAWT models in wind tunnels employing active drive mode to ensure more effective self-starting and cut-in threshold features, extended operating range, and minimize friction losses. Experimental results obtained using H-type three-bladed VAWT were adopted to consider the blockage effects in the wind tunnel for the solidity of the relevant specimen. An identical restricted design of the turbine was developed using 2D URANS, the numerical performance curve was compared with the experimental results and a remarkable agreement was achieved. A. Subramanian et al. [38] simulated Darrieus VAWT with 1-2.5 TSR values with different airfoils and solidities. Their 3D simulations showed that NACA 0030 has a higher power coefficient at lower values of TSR due to relatively less flow separation, whereas NACA 0012 presented a better performance at TSR > 1.8. The influence of solidity on the performance of VAWT was also examined by M.A. Miller et al. [39], in a study conducted with experimental torque measurements of a turbine varying number of blades ($2 \leq N \leq 5$). The results for high solidity turbines showed that the formations causing the reduction in power related to viscous effects are independent of both TSR and solidity, the role of TSR only resulting in changing the relative wind speed and hence Re_c at the rotor blade. On the contrary, the solidity and TSR influence its maximum performance at high Reynolds number flows.

It was offered as a CFD model by M. Raciti Castelli et al. [40] for simulating power achievement and aerodynamic effects applied on a Darrieus-type wind turbine. The fundamental concepts presently employed in BEM theory for reliable estimation of rotor outcomes have been integrated into the CFD algorithms, enabling the correlation of flow topology properties and dynamic magnitudes. The approach is suggested as a strong construction and optimization method for the advancement of alternative rotor configurations in the deficiency of test data. After defining and verifying the computational

model against experimental results, an entire simulation model is recommended. The flow field characteristics, the variation of time-dependent torque coefficients and relative AoA based on azimuthal position are examined for varied TSRs, presenting a correlation between rotor activity optimized and smaller c_p results, leading to a deeper comprehension of vertical axis wind turbine principal mechanics. The achieved results have demonstrated a decrease in blade relative AoA as TSR values rise, owing to the growing impact of blade translational velocity in the near-blade flow region. Additionally, it has been observed that the highest torque measurements are obtained throughout the turbine is rotating upwind and at azimuthal situations where the rotor blades are subjected to extremely high relative AoA, even following the stall threshold. Even though the mean rotor power coefficient is fairly low, it has been indicated that the power coefficient over time surpasses Betz's limit three times each rotor cycle. This is most likely caused by an abrupt reduction in pressure coefficient that affects the entire rotor disc and the around flow field. Howell et al. [41] performed wind tunnel and 2D and 3D computational analysis on a VAWT with a symmetrical airfoil. According to the torque production and performance coefficient obtained from the experimental data, an increase in performance was demonstrated in higher solidity rotors for two-bladed and three-bladed rotors. While it was observed that surface roughness enhanced performance below Reynolds number of $3x10^4$, it was also pointed out that the power coefficient degraded below this Re number. The existence of the large tip vortices found in both the actual turbine and the three-dimensional analysis was revealed to be the primary reason why the 2D simulations performed substantially better than the 3D simulations. Li et al. [42] compared the precision and reliability of 2D and 2.5D URANS for the aerodynamic concept of VAWT by emphasizing the capacity of the 2.5D LES approach at high AoA flow. In comparison to preceding experimental findings, the 2.5D LES approach has been suggested as a more accurate and efficient CFD application than the other two approaches in conjunction with investigating the aerodynamic parameters of VAWTs. Rezaeiha et al. [43] conducted a comprehensive analysis to evaluate the accuracy of various eddy-viscosity turbulence models for Reynolds-Averaged Navier-Stokes (URANS) of VAWTs, employing seven turbulence models. These turbulence models were validated with experimental results [18,35,40] and the compatibility of the models was evaluated by considering the wake region, the power performance, and the aerodynamic features of the blade. In estimating the specifics of the VAWT's vortex development in velocity profiles with different flow phenomena in the optimum operating circumstance, and the turbine power coefficient over a wide range of TSRs, the SST model versions show a conceivable alignment with these

experimental studies. Thus, the SST-derived models are reported to be the strongest precise within the models assessed for URANS simulations of VAWTs. Besides, the transitional SST variants will be the preferred models thanks to their inherent capability to define the transition on the blade surface during the transitional flow regime (about $Re_c = 2.5x10^5$). The other models were not satisfactory in estimating the power coefficient. [44] offered a precise technique for estimating the continuously varying AoA according to velocity flow field measurements at two reference regions upstream of the turbine blades. Both the fixed pitch and the sinusoidal variable pitch VAWT structures were analyzed with the AoA estimation method, and the fixed pitch was compared with its sinusoidal variable counterpart. Their studies purposed that the sinusoidal variable pitch configuration improved the performance of the turbine.

As mentioned before, the purpose of using active and passive control elements is to enhance the efficiency of the wind turbine blade by raising the lift coefficient and diminishing the drag coefficient. Vortex generators, which are passive flow control methods, were first documented by Taylor [45] and have been the subject of study by many researchers until today, especially for preventing flow separation, which directly affects aerodynamic performance [46,47]. Another passive flow control method, slats mounted on the leading edge of the airfoil, was explored in 1933 by Weick and Shortal [48] and is a charming method examined by aerodynamics researchers ever since [49,50]. In addition to delaying the flow separation, these devices result in the creation of more lift than the turbine airfoil without any control element, especially at high AoA. The protuberance employed on the leading edge of the turbine blade profiles, inspired by the flippers of humpback whales, is also employed to suppress flow separation. These protuberances on the airfoils provide 3D flow occurrences that delay the flow separation event while increasing velocity and consequently momentum value to the flow [51,52]. Ismail et al. [53] computationally employed the dimple and Gurney flap at the blowing surface of the NACA 0015 airfoil and investigated its effect on the average torque of the VAWT. To enhance the torque output of the wind turbine blade, a completely automatic optimization was applied. The data required for the optimization method, particularly at relevant TSR were obtained by CFD simulations, verifying with previously reported experiments.

Apart from these studies on the passive control methods, Koca et al. [54-57] focused on the NACA 4412 airfoil, interfering with the flow with sandpaper instead of the vortex generator.

The LSB that forms on the airfoil profile and negatively affects aerodynamic performance is lessened and the lift force is raised by applying sandpaper to the airfoil surface corresponding to the 15%-25% chord length of the airfoil, as shown in Figure 2.1.

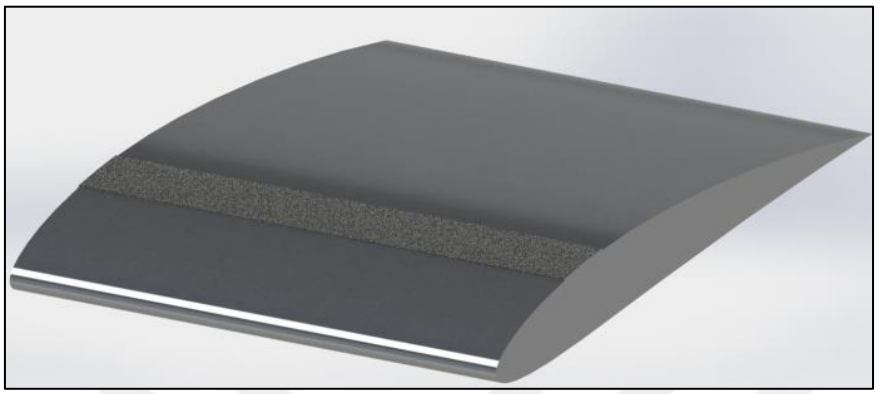

Figure 2.1. NACA 4412 airfoil with sandpaper on the upper surface [57]

The effects of isolated, cylindrical roughness devices on the transition boundary layer are examined and compared to global linear stability by Puckert et al. [58]. Experimental measurements were conducted as measurements techniques over a flat plate in a water channel to provide experimental verification of global instability. Their research revealed that roughness wake dynamics demonstrated a variety of cases at different Reynolds number ranges (such as around the critical Reynolds number). The placing of a surface roughness device over an actual wind turbine blade [59], as shown in Figure 2.2, favourably affected the power output of a real wind turbine.

Figure 2.2. Roughness device employed on an actual wind turbine blade [59]

Zhang et al. [60] proposed a new approach to accurately consider the effect of roughness surface on transition and LSB in turbomachinery flows by the development of a novel transport equation for the roughness amplification factor Ar. Their new models consisting of the combination of a transport equation for the A_r and an intermittency transition model showed good consistency in predicting the onset of transition over rough surfaces for flat

plate, low-pressure turbine vane and high-pressure turbine vane. The findings revealed that the rough wall stimulates the bypass transition and diminishes the length of LSB or even hinders it.

3. DARRIEUS-TYPE VERTICAL AXIS WIND TURBINE AND LOW REYNOLDS NUMBER FLOW FUNDAMENTALS

3.1. Darrieus-Type Vertical Axis Wind Turbine

Due to the advantages of VAWT mentioned earlier, significant advancements remain to be accomplished in the knowledge of it utilizing CFD and experimental techniques to gain deep insight into aerodynamic characteristics and design parameters of VAWTs. A H-type Darrieus VAWT model and the aerodynamic properties of its cross-section are presented in Figure 3.1. The azimuthal angle (θ) specifies the location of the certain blade during its rotation. The unaltered wind speed found in the upstream region of the rotor before encountering the VAWT is known as the free-stream wind velocity, or V. The area of the rotor where the front of the VAWT rotor has had an impact on the flow is known as the downstream region of the rotor. The following is a description of the aerodynamic forces and mathematical. definitions which govern a VAWT's aerodynamic characteristic, as seen in Figure 3.1.

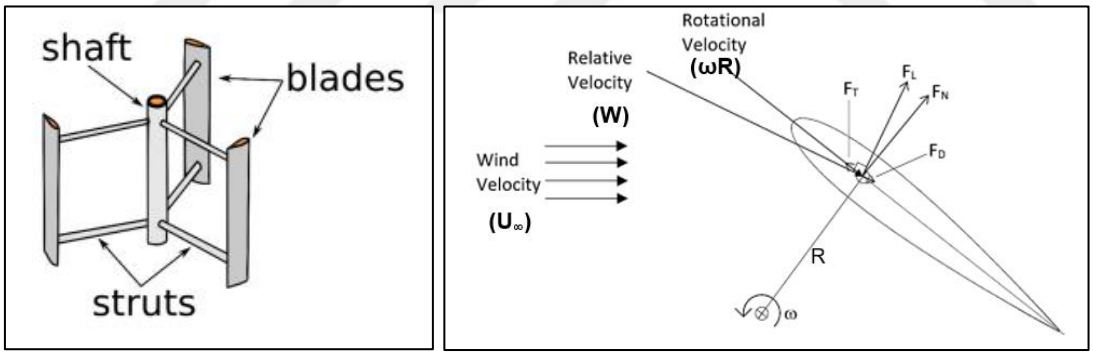

a) b)

Figure 3.1. A sketch of a) a model of three-dimensional straight-bladed VAWT [61], b) the components of velocity, the force components on one of the blades at a relative AoA, α [62]

The relationship between the rotational speed and freestream wind velocity can be stated by the tip speed ratio (TSR) λ, which indicates the rotational speed of the rotor relative to the freestream wind speed:

$$\lambda = \frac{\omega R}{U_\infty} \tag{3.1}$$

where ω is the angular velocity of the rotor, R is the rotor radius, and U_∞ is the freestream wind speed.

The geometric assessments of force components acting on one blade of the turbine are shown in Figure 3.1. The relationship between these forces is shown in Equation 3.2. and Equation 3.3. The normal force F_N and a tangential force F_T were expressed as following equations depending on the lift force F_L and drag force F_D.

$$F_N = F_L cos(\alpha) + F_D sin(\alpha) \quad (3.2)$$

$$F_T = F_L sin(\alpha) - F_D cos(\alpha) \quad (3.3)$$

The blades of a VAWT rotate around an axis with a rotational speed, ω, as indicated in Figure 3.1.b.

The relative velocity (W) that each blade perceives is given by the following formulation (3.4), varying in magnitude continuously:

$$W = U_\infty \sqrt{1 + 2\lambda cos(\theta) + \lambda^2} \quad (3.4)$$

The angle between the relative velocity direction and the chord of the airfoil known as the angle of attack (α), can be written as:

$$\alpha = tan^{-1}\left(\frac{sin(\theta)}{cos(\theta) + \lambda^2}\right) \quad (3.5)$$

As flow comes to the blades and the relative velocity affects the blade surface, aerodynamic forces are created, resulting in a tangential force (F_T) in the VAWT that generates the torque coefficient (C_t). These aerodynamic forces are lift force (F_L) and drag force (F_D), and can be nondimensionalized to obtain the lift coefficient C_L and drag coefficient C_D, respectively:

$$C_L = \frac{F_L}{0.5\rho AW} \quad (3.6)$$

$$C_D = \frac{F_D}{0.5\rho AW} \quad (3.7)$$

where, ρ is the air density, A is the blade area and is the result of multiplying the chord length (c) by the span length of blade (H).

According to the resultant lift and drag forces acting on the blade, the normal force coefficient C_N and the tangential force coefficient C_T can be written as follows:

$$C_N = C_L\, cos(\alpha) + C_D sin\,(\alpha) \tag{3.8}$$

$$C_T = C_L\, sin(\alpha) - C_D cos\,(\alpha) \tag{3.9}$$

The tangential force provides a torque Q, which is the power resource of the VAWT. The power coefficient is explained as the ratio of the power generated by the wind turbine to the power accessible from the wind flow. To determine the aerodynamic performance of VAWTs, it was considered the torque coefficient C_Q and power coefficient C_P provide a reasonable assessment for different VAWTs:

$$C_Q = \frac{Q}{0.5\rho ARU_\infty^2} \tag{3.10}$$

$$C_P = \frac{P}{0.5\rho AU_\infty^3} \tag{3.11}$$

where P is the power, Q is torque, ρ is the air density, R is the rotor radius, and A represents the swept area.

The coefficient of power (C_p) and the coefficient of torque (C_Q) are connected by:

$$C_P = \lambda\, C_Q \tag{3.12}$$

The solidity parameter of the designed turbine, which is the ratio of the open area swept by the rotor to the solid area:

$$\sigma = \frac{N\, c}{D} \tag{3.13}$$

where N is the blade number, c is the airfoil chord length, and D is the rotor diameter.

Betz's law, which explains the constraint on the efficiency of wind turbines, proposes the maximum power that can be converted from wind energy to mechanical energy. By Betz's theory, in ideal circumstances, the highest ratio of energy harvested by the wind turbine from the wind kinetic energy is no greater than 16/27 (about 60%), which is referred to as Betz limit for C_p as shown in Figure 3.2.

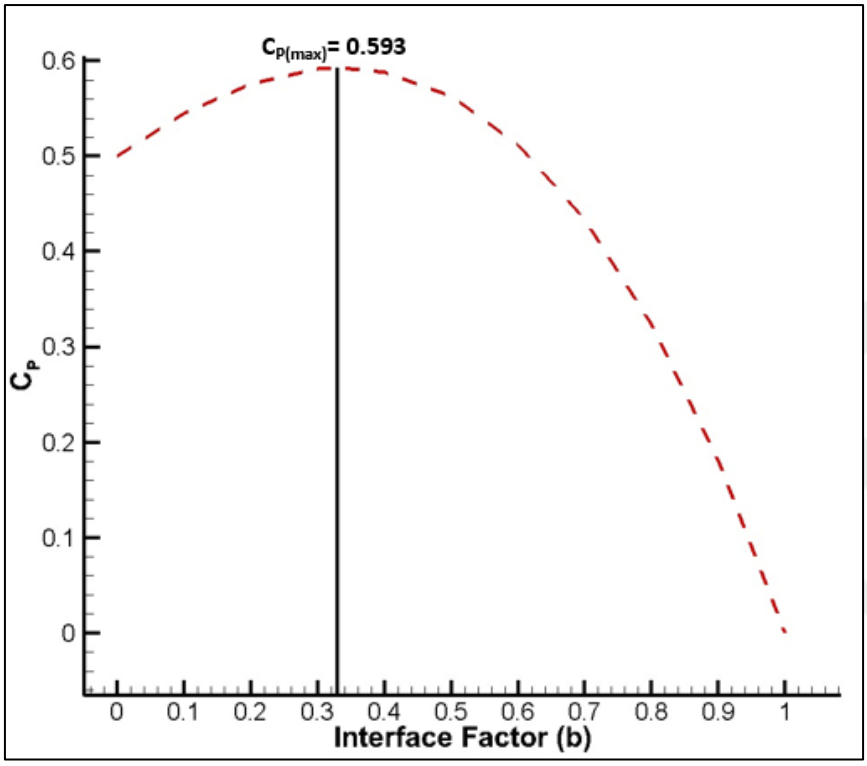

Figure 3.2. The performance coefficient C_p as a function of the interference factor b

3.2. Low Reynolds Number Flow

The Reynolds (Re) number, which is an important dimensionless parameter in identifying flow type, is high in aircraft with high speed. However, because of the short chord length of the blade and the low flow velocity in vehicles such as wind turbine blades and unmanned aerial vehicles, the aerodynamic occurrences in these vehicles differ from the aerodynamic events in high-velocity aircraft. In vehicles such as wind turbines with low Re numbers, some definitions negatively affect aerodynamic performance, which are not encountered in high-speed vehicles. Since these definitions tend to occur at low Re numbers, the flow structure of it needs to be investigated in detail in terms of aerodynamics to minimize these factors that reduce performance.

The Re number, defined by Osborne Reynolds in 1883, is the ratio of inertial forces to viscous forces and is an important dimensionless number that possesses a crucial role in defining the flow type. In an airfoil specified as chord length c, the Reynolds number is defined as follows:

$$Re = \frac{\rho V c}{\mu} \tag{3.14}$$

where Re is Reynolds number, ρ is the air density, c is chord length, and μ is dynamic viscosity.

The operating range of vehicles with a low Re regime is in the range of $5x10^4$<Re< $1x10^6$. The aerodynamics of flows in this range are defined as low Re number aerodynamics [63]. Since viscous forces are effective in low Re number flows, the airfoil passes stall earlier than in high Re number flows.

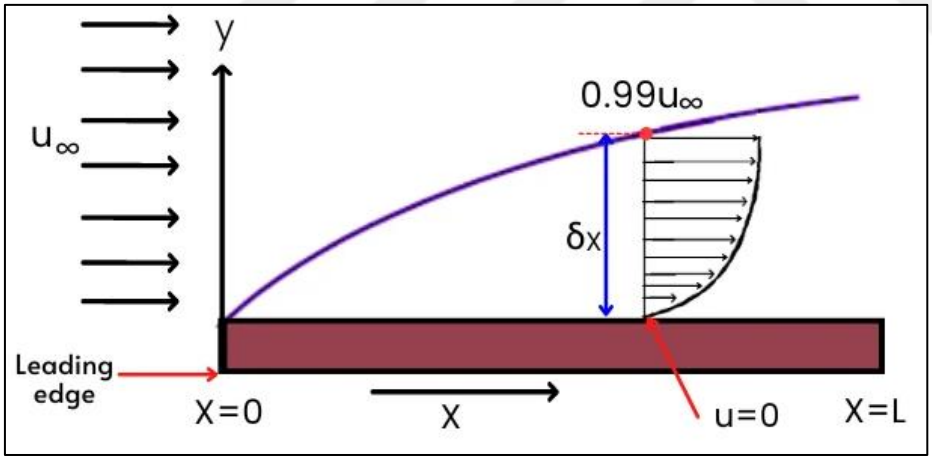

Figure 3.3. The illustration of the boundary layer thickness

Depending on the increase in the local Re number, the flow passes into the turbulent transition zone and the flow starts to become unstable compared to the laminar zone. Finally, the flow comes into the turbulent region, where the flow becomes completely chaotic. The boundary layer thickness (δ), a function of the Re number and was represented in Figure 3.4.

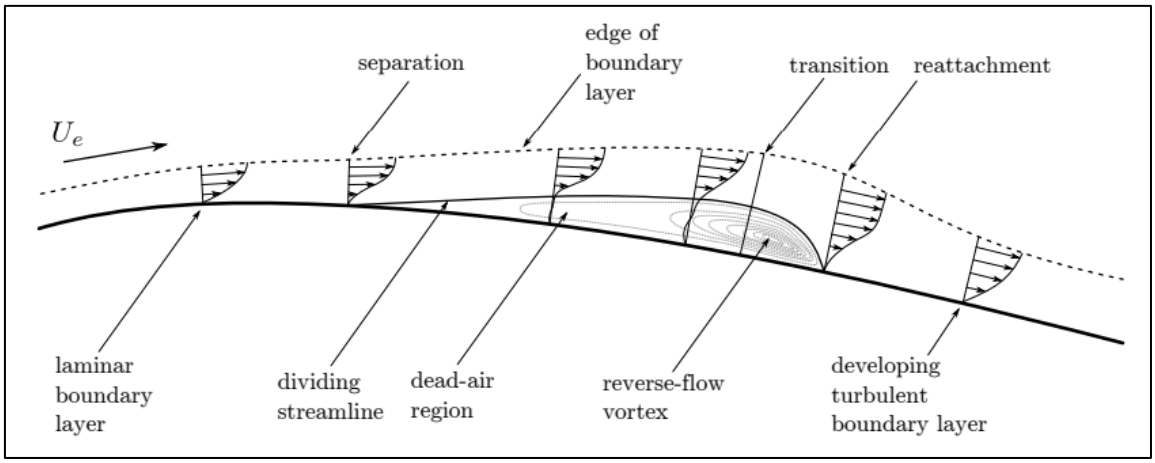

Figure 3.4. The sketch of the time-averaged illustration of a laminar separation bubble [64,65]

LSB, which is a low Re number aerodynamic phenomenon, can cause disturbing noise and vibrations as well as affect aerodynamic performance [67,68]. As the formation of the LSB, the laminar flow at the beginning of the airfoil starts to separate from the surface with the effect of viscous forces that dominate according to the inertia force as it moves towards the trailing edge of the airfoil.

As seen in Figure 3.5, as the pressure coefficient graph of the bubble flow is examined, the LSB on the airfoil and the hump on the pressure coefficient graph show consistency. LSB forms due to viscous forces and adverse pressure gradients acting on the flow in the turbulent transition zone. The point where the laminar separation starts on the airfoil corresponds to the beginning of the hump on the pressure coefficient graph, while the re-attachment of the flow to the airfoil surface means the end of the hump. The point where it peaks in the graph of the pressure coefficient to the hump is also expressed as the transition point. The flow in the LSB on the airfoil has a rotating flow, and this region is also termed the dead air zone in the literature [69]. The velocity in the swirling flow section in the dead air zone is almost zero, so the pressure difference is negligible.

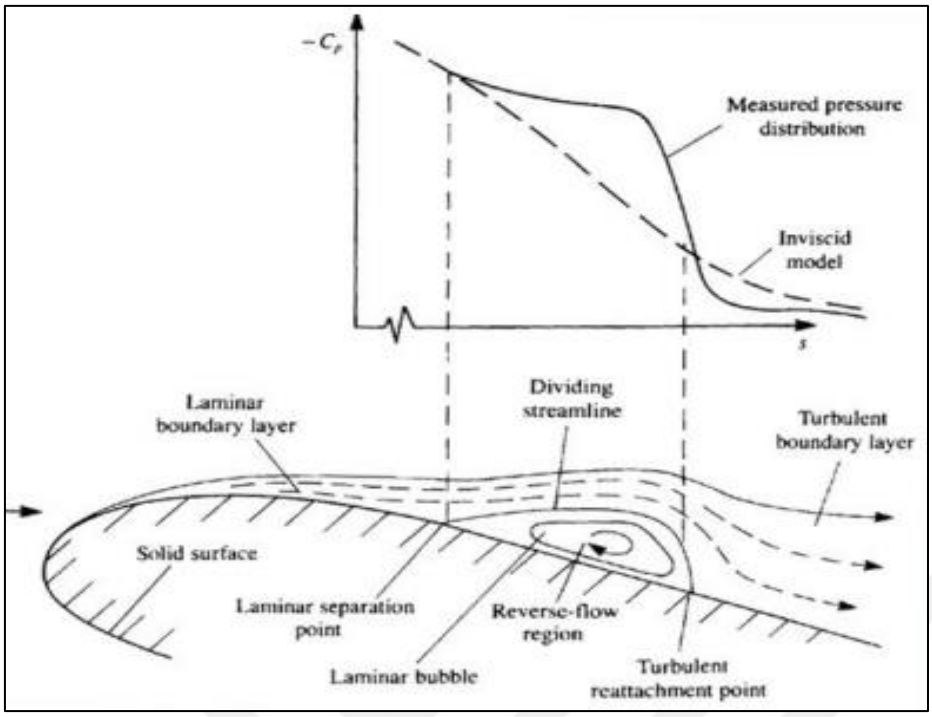

Figure 3.5. The influence of a laminar separation bubble on pressure distribution [70]

A short bubble is formed when the flow separates the surface and immediately reattaches to the surface, gaining adequate momentum. But in some cases, the flow reattaches to the surface after a certain period depending on flow characteristics. In this case, a long bubble occurs on the airfoil. If the transition takes place lately in flow, instead of long or short bubbles, the flow cannot reattach on the surface and a stall occurs as indicated in Figure 3.6.

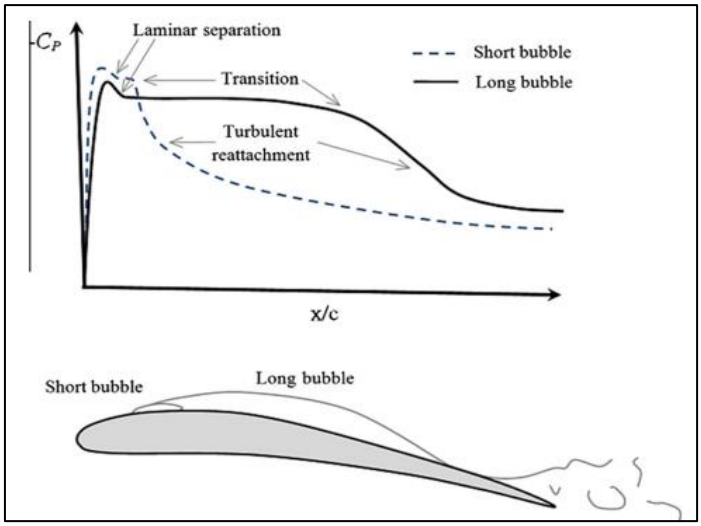

Figure 3.6. The pressure distribution on an airfoil is a result of the formation of a short and long separation bubble [66]

As the laminar separation bubble has been investigated in depth aerodynamically, its location on the blade has a significant impact on performance. Because flow control is required to reduce the effects of laminar separation bubbles, which is an undesirable situation.

4. MODEL DESIGN AND NUMERICAL METHODOLOGY

According to the literature review, the NACA 0018 airfoil, which is frequently used in turbine applications and can be compared both experimentally and numerically, was chosen. It is aimed to elaborate numerically on the flow characteristics around the small-scale VAWT via Computational Fluid Dynamics (CFD).

NACA 0018 which is a symmetrical (maximum camber 0% at 0% chord) airfoil has a maximum thickness of 18% chord length as seen in Figure 4.1.

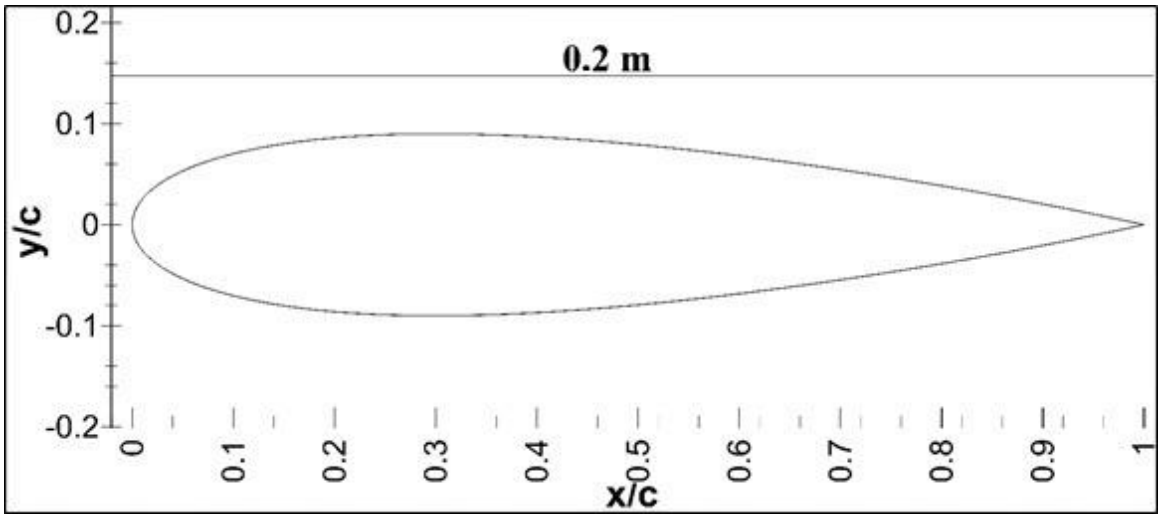

Figure 4.1. The sketches of the NACA0018 airfoil used in the present study

The VAWT model has three straight blades with 0.2 m chord length at a radius of 0.4 m from the central shaft. The numerical analysis was performed at an angular velocity of 18.75 rad/s corresponding to a TSR of 0.75 to compare with the experimental study [33,34].

In numerical analysis, the mesh quality is an important part as well as validation with the experimental study. Since the flow over the wind turbine should not affect the wall or other boundaries, the flow domain is far enough from the turbine model. The numerical domain and mesh grid was created in GAMBIT software as shown in Figure 4.2. In this study, the diameter of the flow domain was selected as 160c, and the rotating domains were drawn separately.

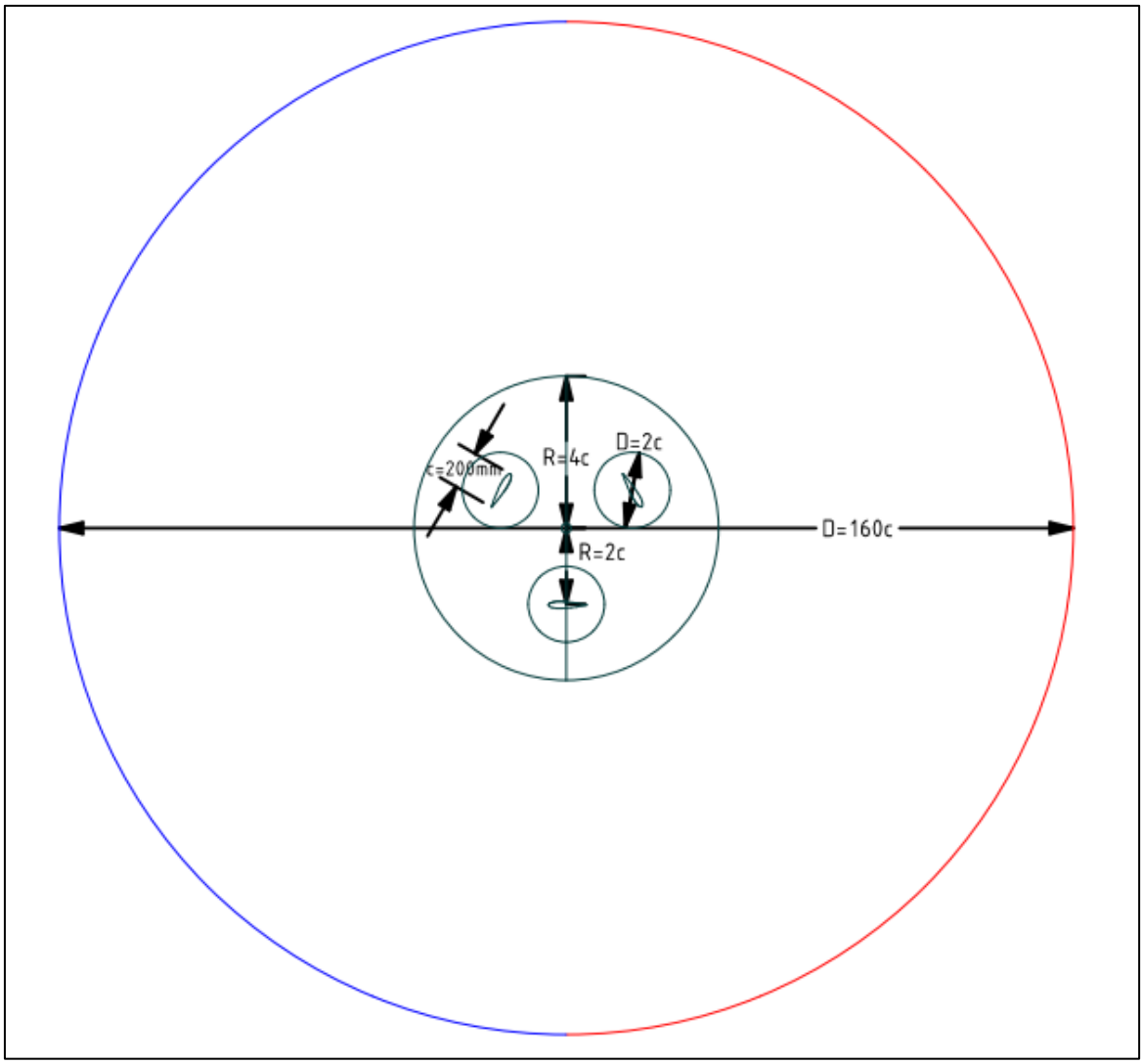

Figure 4.2. Geometrical definition of VAWT model in the present study

Turbulent flows are identified as fluctuations in velocity fields. These fluctuations cause convection quantities such as momentum, energy and mass density to change. Because these variations are of small scale and high frequency, it is very difficult to directly model these fluctuations in engineering calculations. Instead, instantaneous general equations are defined as Reynolds Averaged Navier-Stokes (RANS) so that minor scales are removed from the equations, resulting in modified equations for less costly solutions. This phenomenon is called turbulence analogy and it comes with new assumptions and approaches. Numerical analysis is a list of many assumptions. Different turbulence models have been revealed by using theoretical and experimental data in turbulence simulations [71,72]. A single and agreed model that can comprehensively solve all flow problems does not yet exist in practice. Factors such as the flow physics of the surrounding environment, the level of accuracy, and

the capacity of the computers to be used are important in the settling of the turbulence model. Although laminar flows could be easily solved by using CFD in numerical solutions, it is necessary to solve turbulent flows in practice using turbulence models. Since the simulation models are not sufficient for current low Reynolds number flows, the transition SST model was used in VAWT modeling in the thesis study.

In this study, simulations were performed in the academic-based ANSYS Fluent software based on the Control Volume Method. The SIMPLE Solution algorithm and the Second Order Upwind discretization approach have been selected. Transition SST turbulence model has been chosen for the numerical simulations, allowing for virtually defining the roughness height to the surface. The airfoil surface was separated locally, for different distances depending on chord length.

RANS equations for incompressible flow;

$$\frac{\partial \overline{u}_i}{\partial x_i} = 0 \tag{4.1}$$

$$\frac{\partial \overline{u}_i}{\partial t} + \frac{\partial}{\partial x_j}\left(\overline{u}_i \overline{u}_j\right) = -\frac{1}{\rho}\frac{\partial \overline{p}}{\partial \overline{x}_i} + \frac{\partial}{\partial x_j}[\nu\left(\frac{\partial \overline{u}_i}{\partial x_j} + \frac{\partial \overline{u}_j}{\partial x_i}\right) + \tau_{ij} \tag{4.2}$$

where ν is the kinematic viscosity, $\overline{p}$ is the pressure, ρ is the flow density, ū is the velocity and τ_{ij} is the stress tensor.

The correlation equation [73] used to model the wall roughness in the turbine blade is:

$$Re_{\theta tr} = [\frac{1}{Re_{\theta t}} + 0.0061 f_{\Lambda}\left(\frac{k}{\delta_t^*} - 0.01\right)^{f_{Tu}}]^{-1} \tag{4.3}$$

where Λ is the density parameter used to define the roughness, f_{Tu} is the free flow turbulence effect. Also, the flow over the roughness has been modified for this model and the following equation 4 has been integrated [74];

$$Re_{\theta tr} = Re_{\theta t} min\,[1; \frac{0.0554 + 1.005\left(\frac{\theta_t}{k}\right)^{0.87}}{1.4629 + \left(\frac{\theta_t}{k}\right)^{0.87}}] \tag{4.4}$$

With these equations, the roughness was modeled virtually on the blades and the effect of roughness on the flow of VAWT was addressed. In this thesis study, virtual modeling was performed using these correlation equations and it was revealed how the effect of roughness on rotation and aerodynamic parameters of a vertical axis wind turbine.

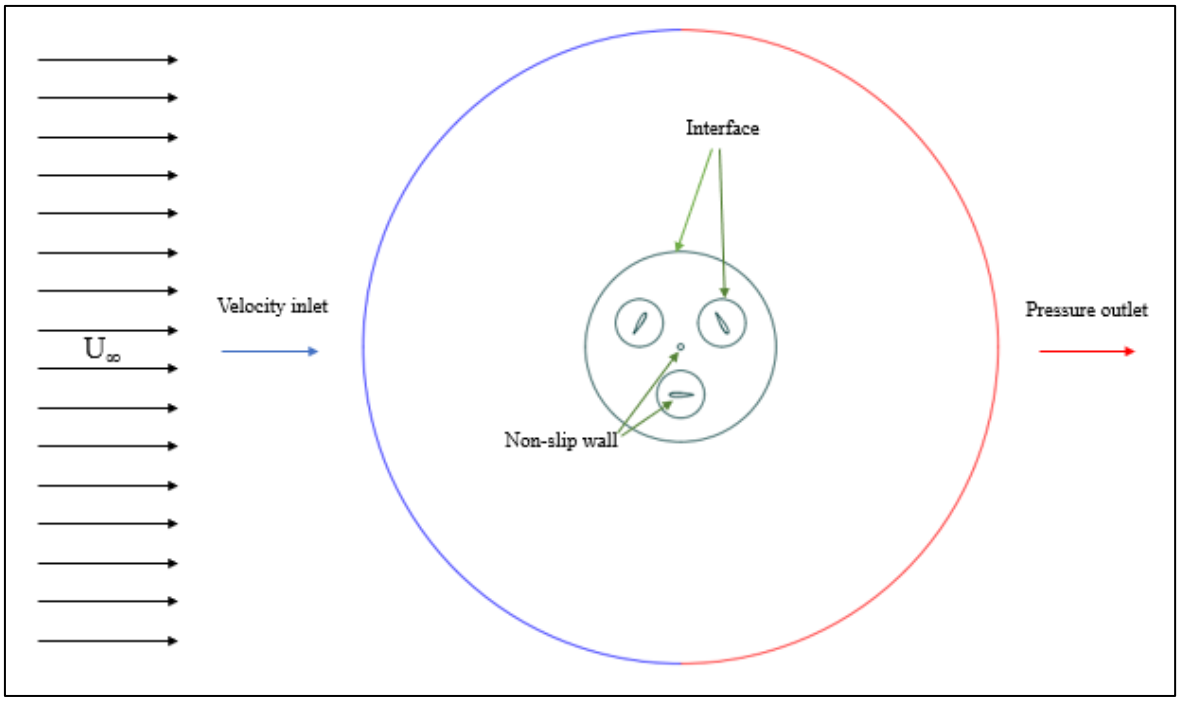

Figure 4.3. Representations of boundary conditions for VAWT computational domain (not to scale)

The velocity inlet boundary condition was defined with the 10 m/s wind speed corresponding to a chordwise Reynolds number of 1.37 x 10^5. The O-type mesh topology was utilized for the stationary domain and rotational region (Figure 4.4). The total node number was approximately 265000. In terms of the residuals, the converge criteria were accepted as O (5). In literature, for CFD simulations that include rotating components, a moving mesh technique is applied, with the interface between the separate sections referred to as the sliding interface. The nearby cells of the sliding interface are relocated at each time step, to regard the rotation. The solver parameters precisely identify the moving and stationary parts of the mesh. Therefore, the stationary and rotational domains connected with the non-conformal interface boundary condition to provide continuity and momentum flux of fluid flow into the rotational domain [75]. No-slip surfaces were used to represent the surfaces of the blades and the shaft to define no-slip boundary conditions. To be able to observe occurring in the boundary layer, a boundary layer mesh was generated around each blade.

Also, the wall distance parameter (y+) and its growth ratio were calculated and y+ was selected as under 1.

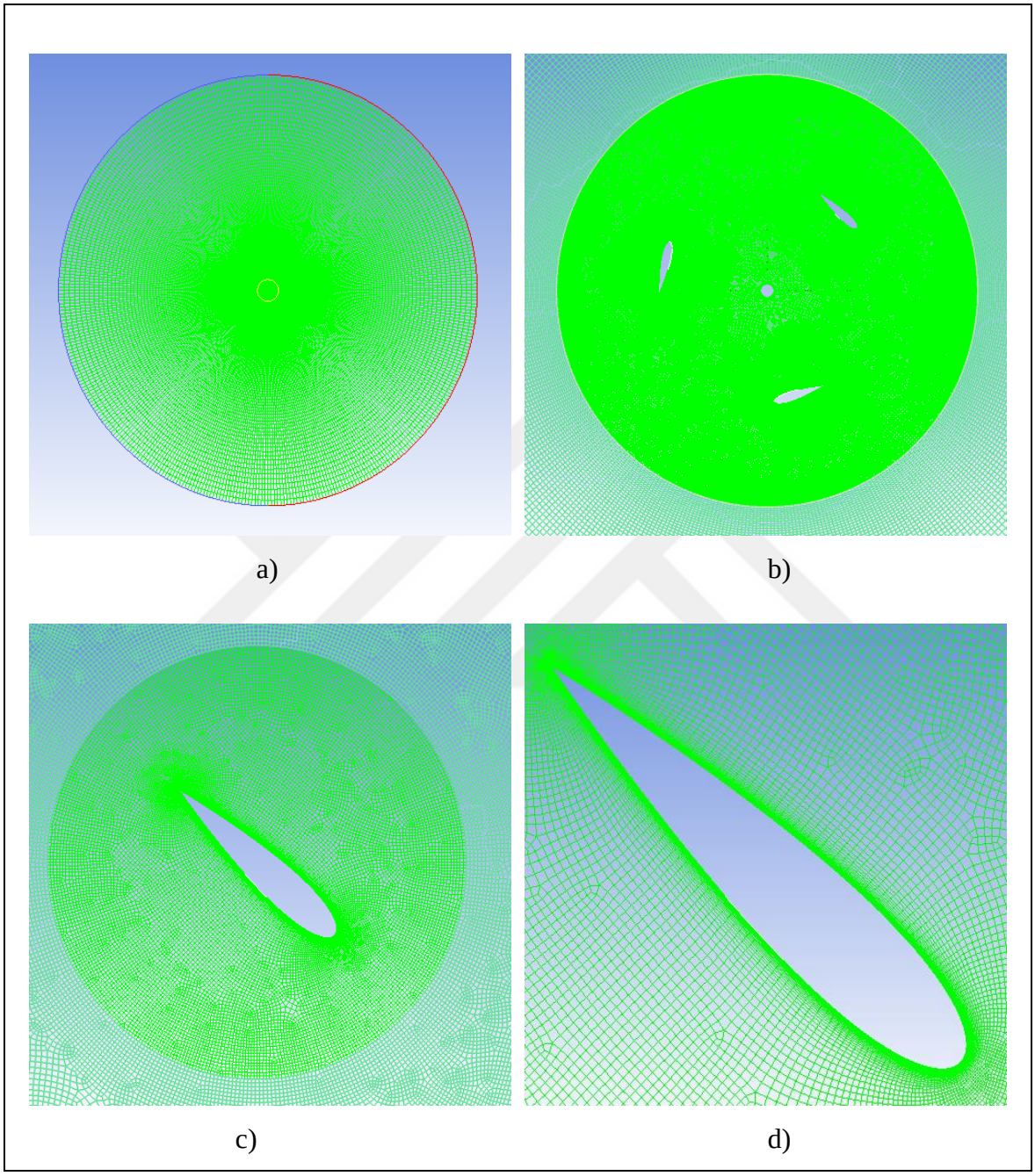

Figure 4.4. Mesh topology for the CFD technique applied to a VAWT, (a) the stationary domain, (b) the rotating region with three-bladed VAWT with NACA 0018 airfoils, (c) mesh topology surrounding the blade, (d) detailed boundary layer mesh around the blade

Table 4.1. Model features and numerical parameters in the present study

Parameter	*Value*	*Property*	*Value*
Blade shape (-)	*NACA 0018*	*Mesh Geometry*	*Structured*
Number of blades (-)	*3*	*Number of nodes*	*265000*
Chord, c (m)	*0.2*	*First layer thickness*	*<1*
Turbine radius, R (m)	*0.4*	*Boundary layer growth rate*	*1.2*
Solidity, σ (-)	*0.75*	*Turbulence model*	*Transition SST*
Rotational speed, ω (rad/s)	*18.75*	*Solution algorithm*	*SIMPLE*
Freestream velocity, U_∞ (m/s)	*10*	*Discretization approach*	*Second Order Upwind*

In this study, the Transition SST turbulence model was employed, which allows us to define the sand-grain roughness height to the walls virtually, as seen in Figure 4.5. After the roughness height was defined, it was dimensioned to the chord length to present more accurate and comparable data. In order to examine the effects of roughness height on the flow of VAWT, different heights (k) were determined as 0.0006 m, 0.0012 m, 0.0018 m, 0.0024 m, which correspond to the dimensionless length k/c of 0.003, 0.006, 0.009, 0.012 respectively [54]. In addition, the wall length specified by the roughness of the airfoil was investigated depending on the chord length as shown in Figure 4.5. The rough airfoil surface has been evaluated in three different ratios of 5% (x/c: 0.10 – 0.15, 0.15 – 0.20, 0.20 – 0.25, 0.25 – 0.30), 10% (x/c: 0.15 – 0.25, 0.20 – 0.30) and 50% (x/c: 0 – 0.50) depending on the chord length. The reason for choosing these cases was to intervene and improve the flow where the laminar separation bubble and leading-edge separations could have occurred on the blades at low Reynolds number flows.

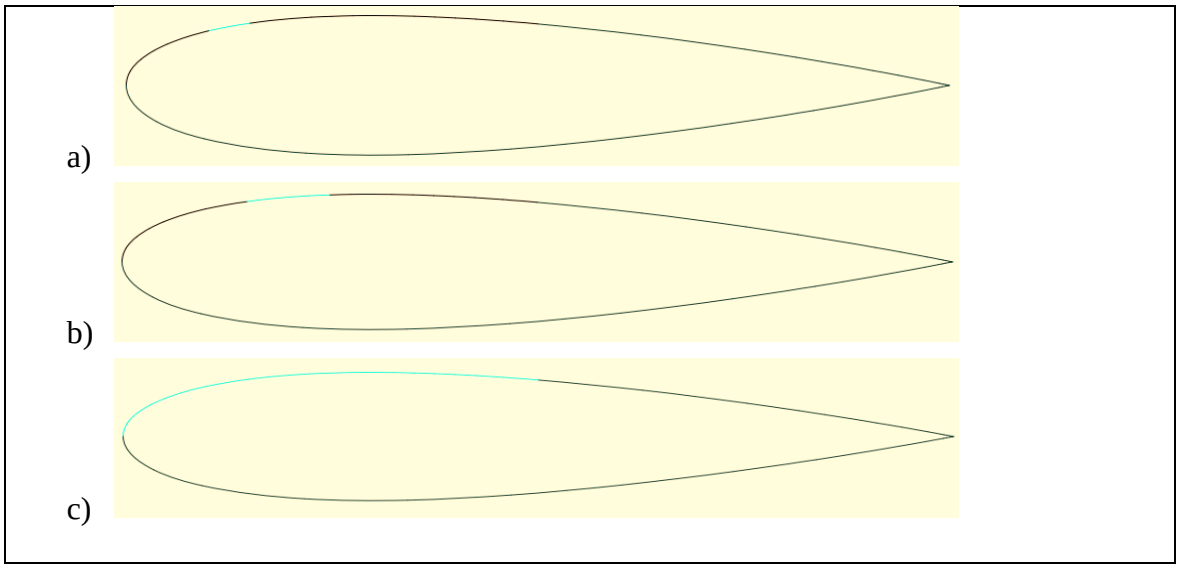

Figure 4.5. Representation of airfoil walls with roughness element at different locations a) x/c: 0.10 – 0.15, b) /x/c: 0.15 – 0.25, c) x/c: 0 – 0.50.

5. RESULTS AND DISCUSSION

5.1. Modelling of VAWT

In this study, the experimental data [33,34] from the literature were compared to computational the outcomes generated from Transition SST model to evaluate the feasibility and reliability of the four-equation γ-Re_Θ (Transition SST) model on VAWT. As a result of the numerical analysis performed at different TSRs, the power coefficient obtained numerically at TSR=0.75 showed the best agreement with the experimental studies with a C_p value of 0.080 as shown in Table 5.1. The discrepancy between the experimental and the simulation results for higher TSRs is predicted to be due to the neglect of rod effects in the 2D simulation. The numerical studies with 2D simulation models are not able to take the connecting rod into account. The rod effect becomes important, especially in increasing TSR values [34]. Consequently, the low TSR numerical value (0.75) considered in this study was consistent with the experimental data, and it is validated. Further studies were continued at this value.

Table 5.1. Comparison of Cp obtained in the present study at TSR value of 0.75 with the studies of Ma et al. [33] and Elkhoury et al. [34]

	C_p value at TSR: 0.75
Present Study	0.080
M. Elkhoury et al.	0.088
N. Ma et al.	0.080

Figure 5.1 shows the x-velocity contours around VAWT and its wake region. In this contour distribution, the airfoils (blades) were at different AoA and thus vortices formed around the blades. The vortices around the front blade affected the other blades, and vortex shedding formed the wake region. In Figure 5.1, it was focused on the blades, and the x-velocity contours were given. The vortex formation and its effect on the flow over the VAWT were seen in Figure 5.1. Since the front blade was vertical to the flow, large vortices occurred. The upper blade was upside down and angled, thus creating large vortices. As a result, these vortices occurred in different regions as the blade angles constantly changed on the vertical axis and affected the rear over blade-flows.

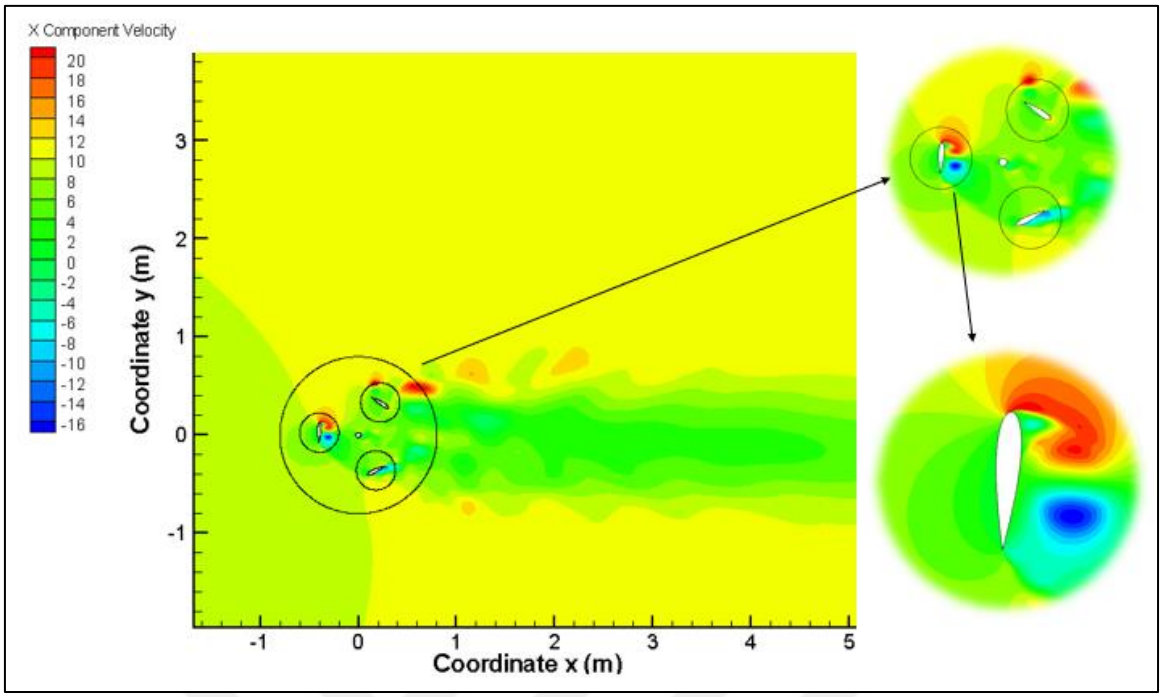

Figure 5.1. The x-axis velocity contours in the full domain, rotational region and around the blade

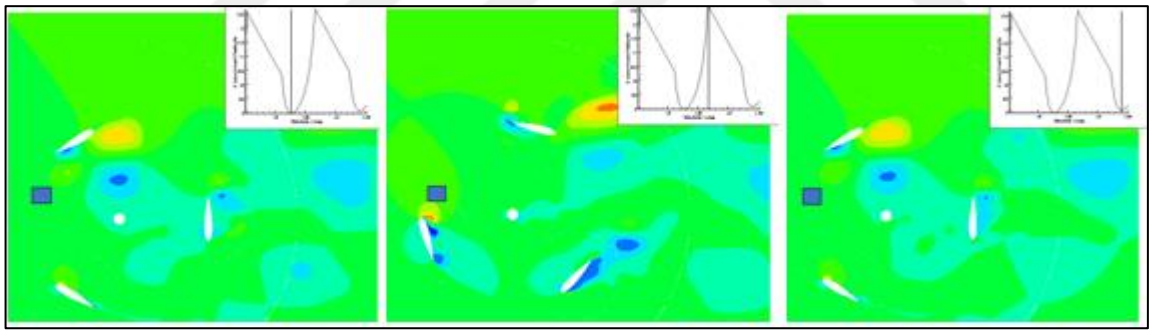

Figure 5.2. Variation of x-velocity at a certain point with time

The x-velocity variation at a certain point over time is shown in Figure 5.2. It was observed that when the blade passed and moved away from the selected point, the velocity was minimum at this point. On the other hand, the blade's leading edge approaching this point caused an increase in speed at this point.

In this study, different roughness ratios and positions over the blade were analyzed. In the first stage, the roughness was tested in small partial areas close to the leading edge of the blade to trigger the transition to turbulence over the blade. As seen in Table 5.1, different small increases in the power coefficient were obtained, to a maximum of 3%. Since these

increased rates are small, then an alternative option was tried to see what would happen if 50% of the chord length was covered with roughness in the region near the leading edge of the blade, and an increase in the power coefficient up to 46% was obtained, and it was seen that the aerodynamic performance of VAWTs increased with the use of roughness in a large area. In the following sections, velocity contours and turbulence characteristics will be examined to see how physics over VAWT has changed with roughness.

Table 5.2. Comparison of power coefficient of VAWT with different roughness

Chordwise roughness ratio on the surface (%)	Roughness location (x/c)	Dimensionless roughness height (k/c)	Power coefficient at TSR=0.75	Variation (%)
0	0	0	0.0806	-
5	0.10-0.15	0.003	0.0818	1.49
		0.006	0.0810	0.49
	0.15-0.20	0.003	0.0816	1.24
		0.006	0.0810	0.50
	0.20-0.25	0.003	0.0818	1.49
		0.006	0.0815	1.12
	0.25-0.30	0.003	0.0828	2.73
		0.006	0.0818	1.49
10	0.15-0.25	0.003	0.0815	1.12
		0.006	0.0820	1.74
		0.009	0.0822	1.99
		0.012	0.0817	1.36
	0.20-0.30	0.003	0.0822	1.99
		0.006	0.0830	2.98
		0.009	0.0823	2.11
		0.012	0.0820	1.74
50	0-0.50	0.003	0.1047	29.90
		0.006	0.1114	38.21
		0.009	0.1155	43.30
		0.012	0.1178	46.15

5.2. Numerical Results of VAWT with and without Roughness Element

The transient modelling of VAWT with a clear blade (without roughness) was conducted in ANSYS Fluent software and the time-dependent power coefficient was given for two cycles as in Figure 5.3. In this graph, the blades run at t=0 and the AoA of the blades were changed over time. The angular velocity of VAWT was 18.75 rad/s (179 rpm), and this meant 120° per 0.1 s. The changing of the AoA affected the flow over the blade and VAWT. In VAWT, the power is produced from the lower blade and the AoA of the lower blade is important. As seen in the graph in Figure 5.3, the changing of the AoA of the lower blade produced the energy output until the blade stalled. After the blade stall, until the following blade (upper blade) produced the power, the power coefficient was decreased due to the flow separations. Furthermore, Figure 5.4 shows the time-dependent power coefficients for VAWT with different roughness cases at TSR = 0.75. As seen in this figure, the small length of roughness application over the blade surface did not affect the flow over the blades, and there is not an important increase in the power coefficients of these cases. Therefore, the length of roughness application over the blade surface was raised to 50%, and its numerical results were presented in the following sub-sections.

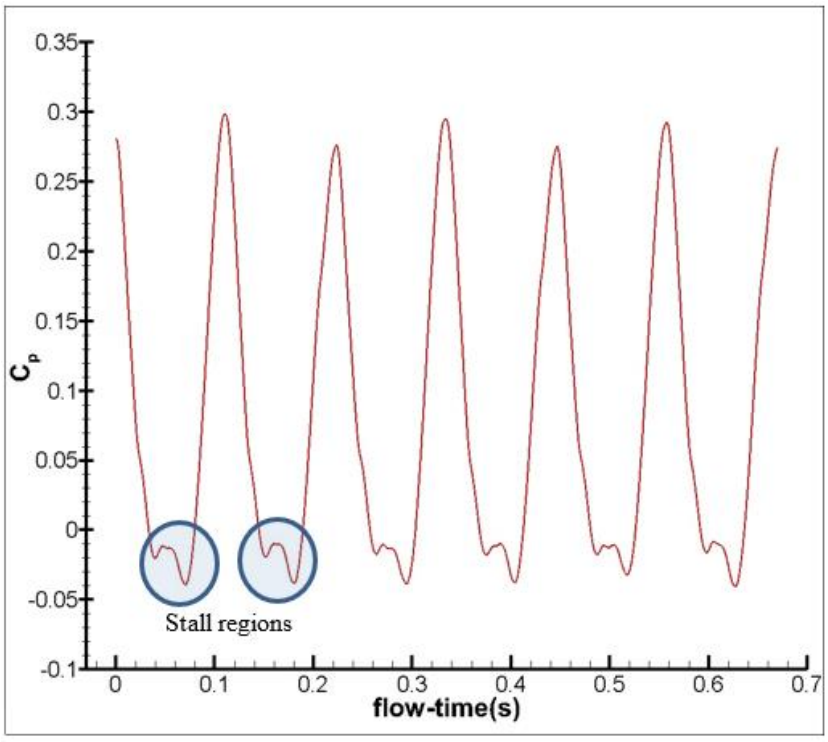

Figure 5.3. The time-dependent power coefficient of baseline VAWT at TSR = 0.75

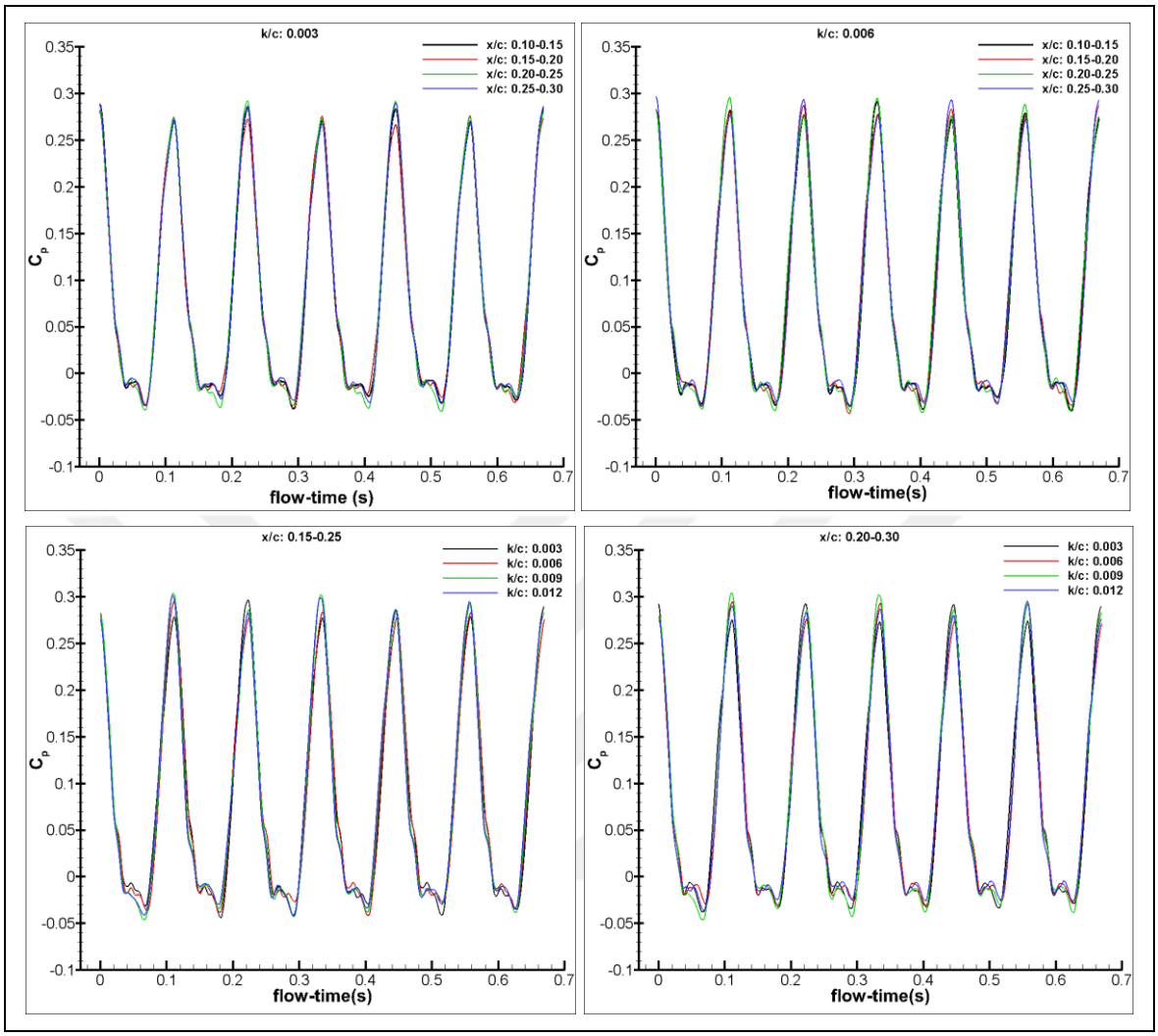

Figure 5.4. The time-dependent power coefficient of VAWT with different roughness cases at TSR = 0.75

5.3. Numerical Results of VAWT for baseline blade without and with the surface roughness ratio: 5%, 10%, 50% cases

The transient numerical results of VAWT with roughness of k/c: 0.006 at different locations was given for two cycles as in Figure 5.5. As seen in the graph in Figure 5.5, as the length of roughness application over the blade surface increased, the time-dependent power coefficient changed, especially at 50%. This change in the length of roughness application over the blade surface positively affected the flow over the VAWT and the power coefficient increased. However, the roughness affected the flow over the lower blade and the deep stall was observed in the lower blade with the changing of the AoA.

The x-velocity (Figure 5.6) and turbulent kinetic energy (Figure 5.7) contours for different roughness lengths were compared with the numerical contours of the baseline blade in Figure 5.6 and Figure 5.7. The vortex formation and its effect on the flow over the VAWT were seen in these figures. Since the front blade was vertical to the flow, large vortices were seen, and turbulent kinetic energy increased in the aft region of the blade. Moreover, as the length of roughness application over the blade surface increased, the vortex formation over the front blade shortened and split. The split vortices and the larger roughness over the blades caused the flow over the lower blade to form a deep stall.

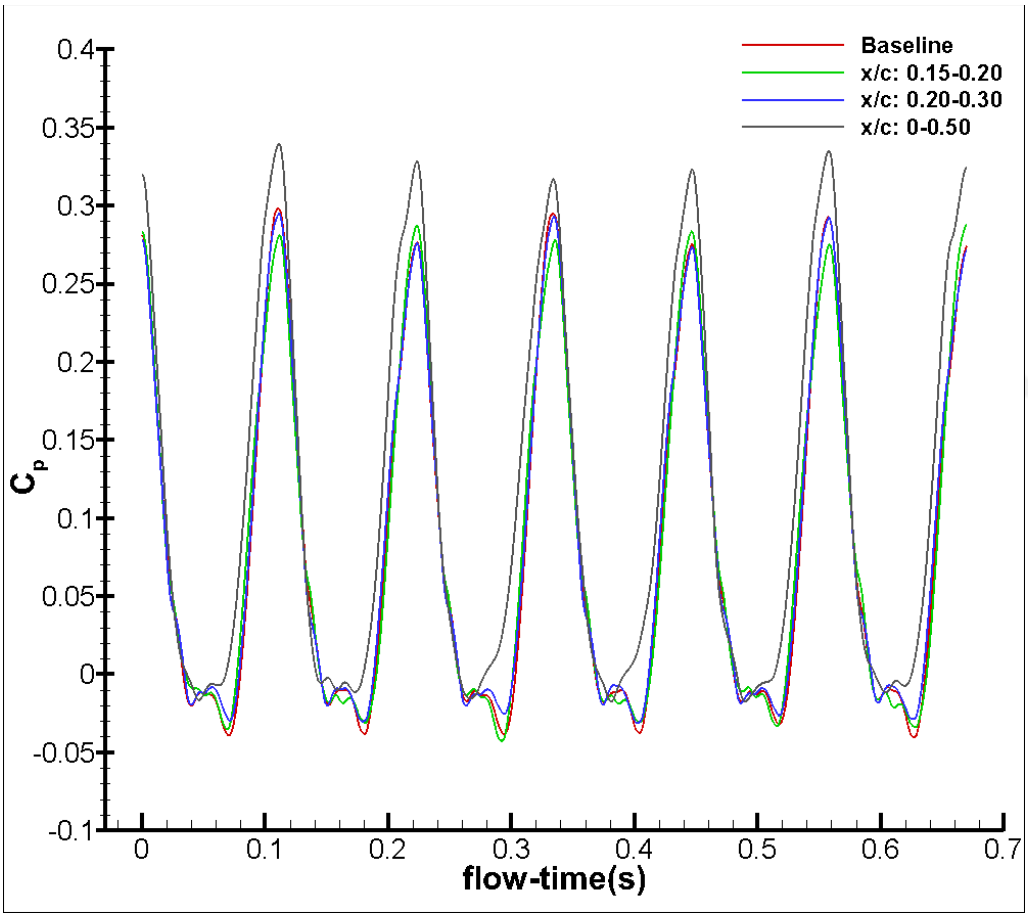

Figure 5.5. The time-dependent power coefficient of VAWT with roughness for k/c: 0 (baseline) and k/c: 0.006 cases at TSR = 0.75

k/c: 0 (baseline)	k/c: 0.006		
	x/c: 0.15-0.20 (5%)	x/c: 0.20-0.30 (10%)	x/c: 0-0.50 (50%)

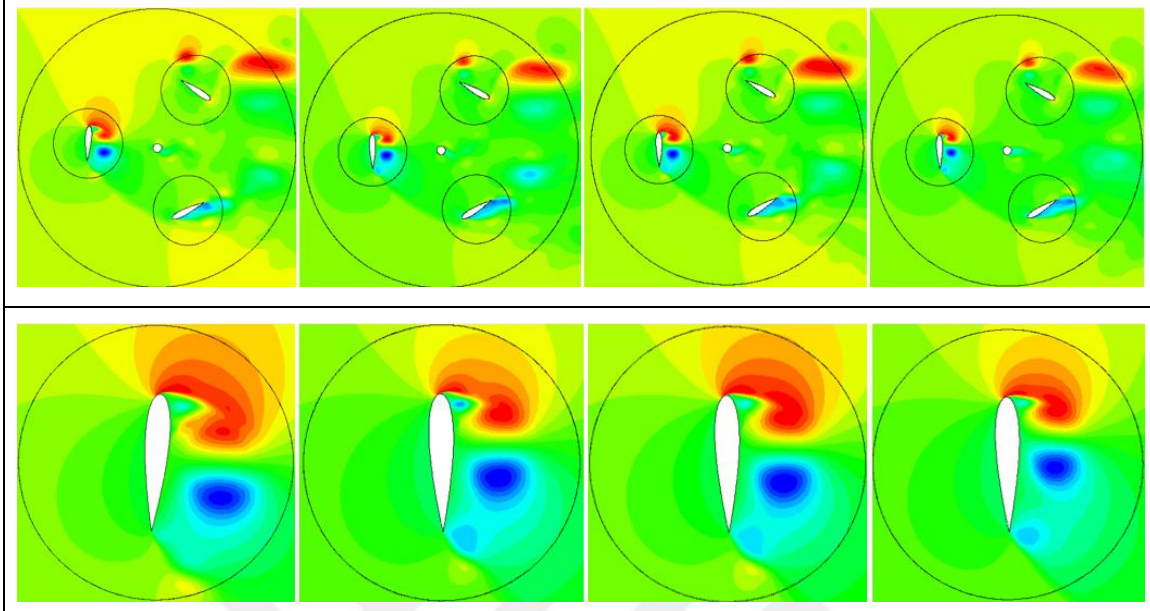

Figure 5.6. The instantaneous x-velocity contours of VAWT with roughness for k/c: 0 (baseline) and k/c: 0.006 cases at TSR = 0.75

k/c: 0 (baseline)	k/c: 0.006		
	x/c: 0.15-0.20 (5%)	x/c: 0.20-0.30 (10%)	x/c: 0-0.50 (50%)

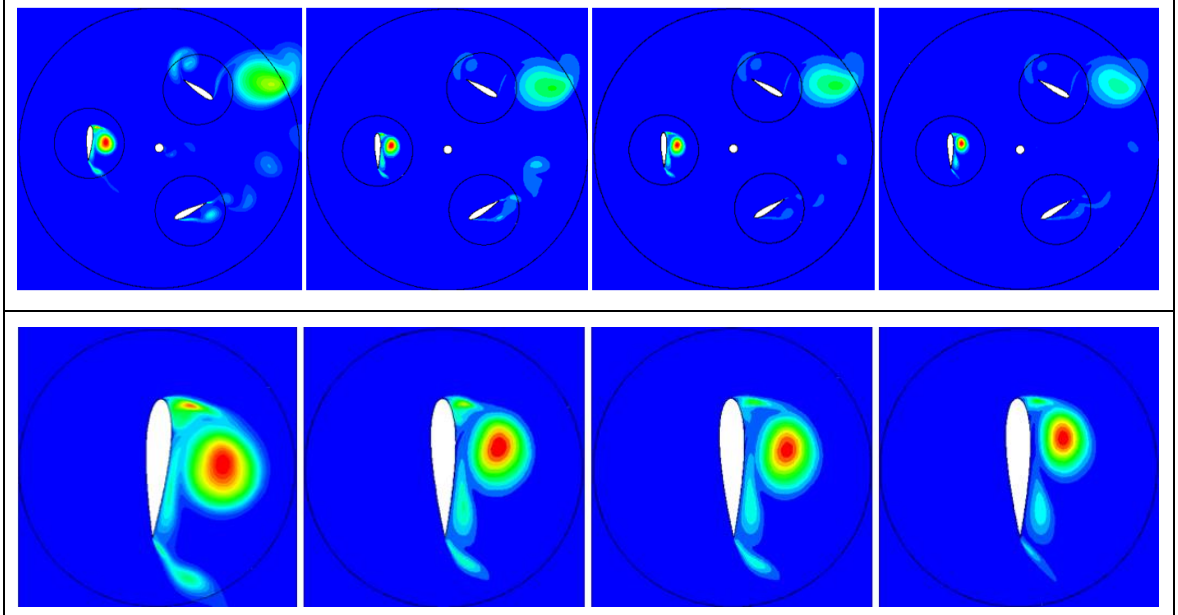

Figure 5.7. The instantaneous turbulent kinetic energy contours of VAWT with roughness for k/c: 0 (baseline) and k/c: 0.006 cases at TSR = 0.75

5.4. Numerical Results of VAWT with the surface roughness ratio of 50%

The length of roughness application over the blade surface was raised, and aerodynamic performance was increased. Therefore, the improvement detail was investigated in this section. The transient numerical results of VAWT with roughness for different k/c ratios such as 0.003, 0.006, 0.009 and 0.012 between x/c=0 and x/c=0.50 was given for two cycles in Figure 5.8. As the length of roughness application over the blade surface prolonged, the time-dependent c_p enhanced. While the pre-stall and then the stall phenomena were seen in the c_p graph of the baseline blade, the stall was observed directly in the power coefficient graph of VAWT with roughness between x/c=0 and x/c=0.50.

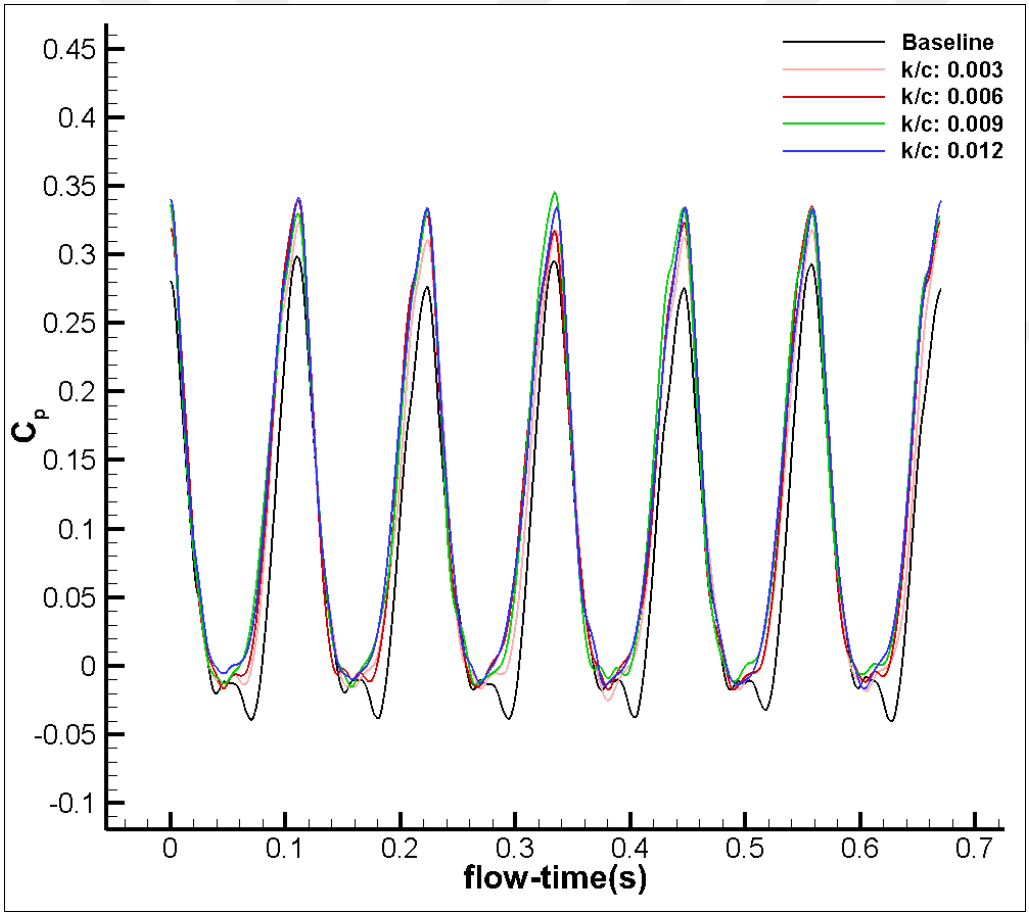

Figure 5.8. The time-dependent power coefficient of VAWT with roughness for different k/c ratios between x/c=0 and x/c=0.50 at TSR = 0.75

The x-velocity and turbulent kinetic energy contours of VAWT with roughness for different k/c ratios between x/c=0 and x/c=0.50 was presented in Figure 5.8 and Figure 5.9. The vortex formations around the blades of VAWT were shown in these figures. As the roughness

height over the blade surface was prolonged, the vortex formation over the vertical blade became evident due to the roughness on the surface. This was seen from the turbulent kinetic energy contours in Figure 5.10.

k/c: 0 (baseline)	x/c:0-0.50			
	k/c: 0.003	k/c: 0.006	k/c: 0.009	k/c: 0.012

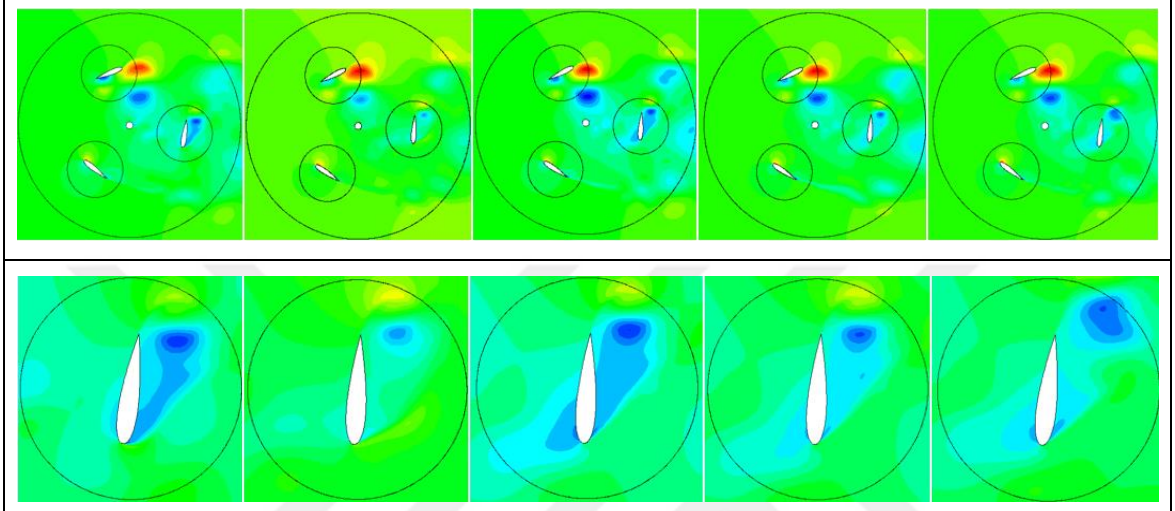

Figure 5.9. The instantaneous x-velocity contours of VAWT with roughness for different k/c ratios between x/c=0 and x/c=0.50 at TSR = 0.75

k/c: 0 (baseline)	x/c:0-0.50			
	k/c: 0.003	k/c: 0.006	k/c: 0.009	k/c: 0.012

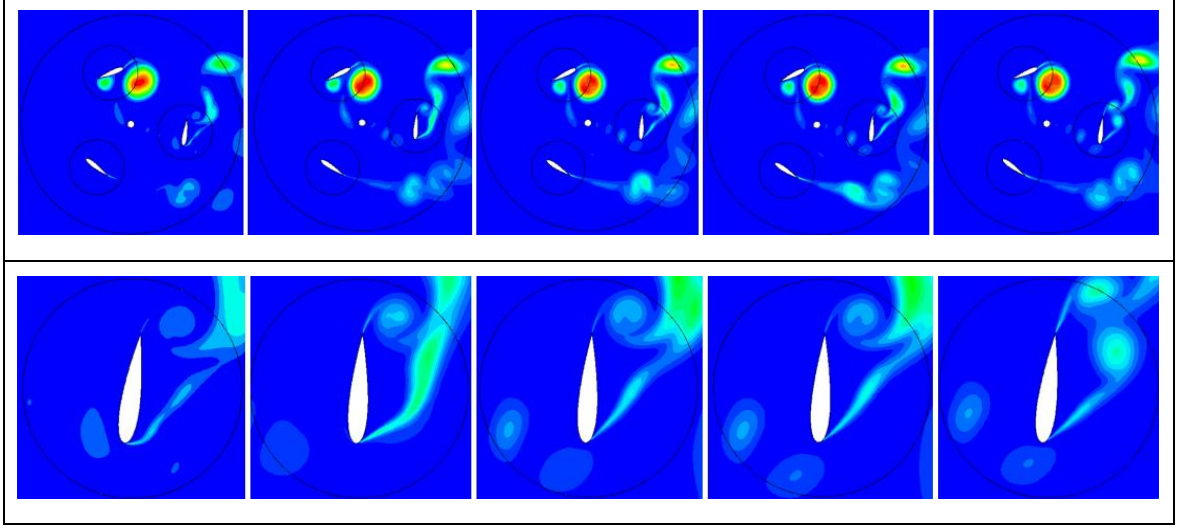

Figure 5.10. The instantaneous turbulent kinetic energy contours of VAWT with roughness for different k/c ratios between x/c=0 and x/c=0.50 at TSR = 0.75.

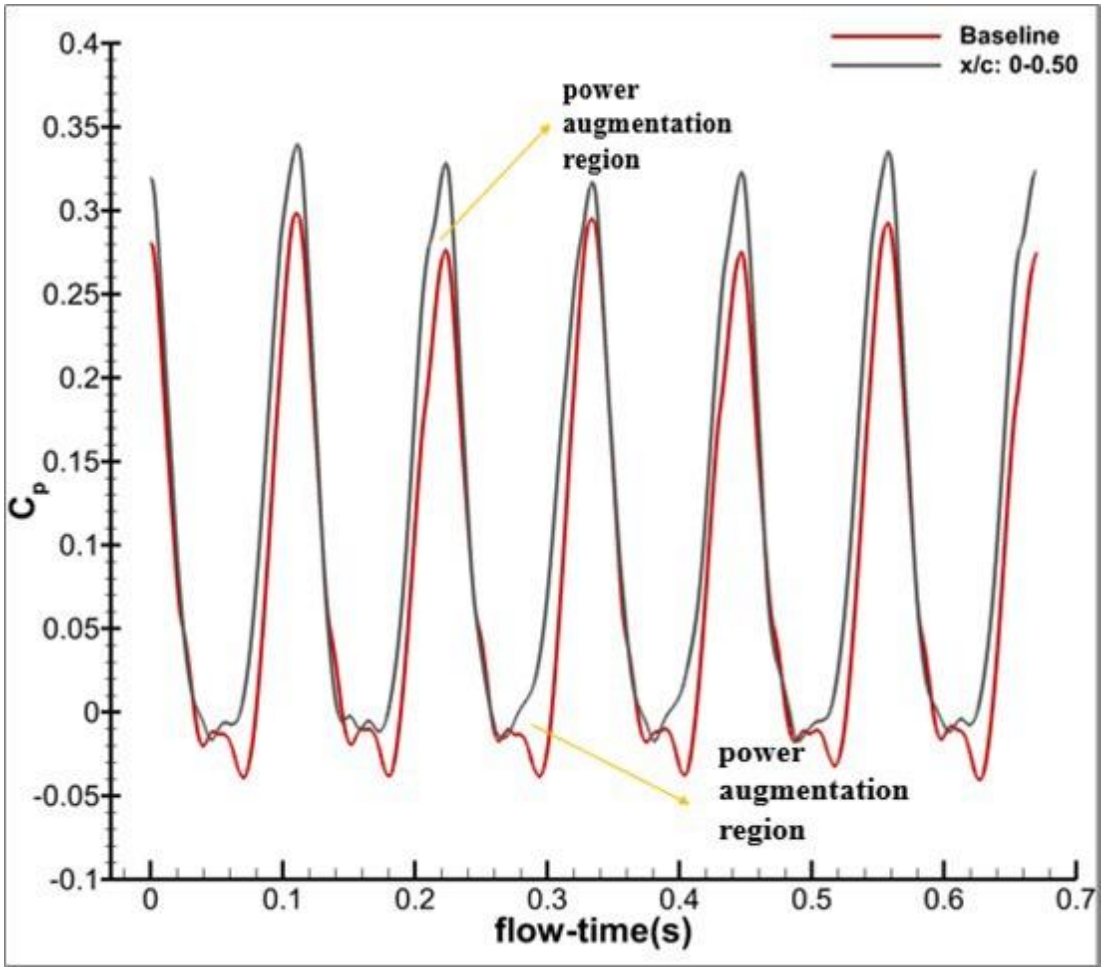

Figure 5.11. The time-dependent power coefficient of VAWT with roughness for baseline and k/c=0.012 between x/c=0 and x/c=0.50 at TSR = 0.75

Time-dependent power coefficient variation has been shown in Figure 5.11 for the baseline VAWT and the controlled VAWT with k/c=0.012 between x/c=0 and x/c=0.50. Especially in the case of flow separation, power augmentation regions evolved as a result of the roughness element providing momentum to the flow. Thus, the flow was reattached to the surface and the LSB was suppressed, increasing the upper peaks of the power coefficient curve, and both an increase and stability in the lower peaks.

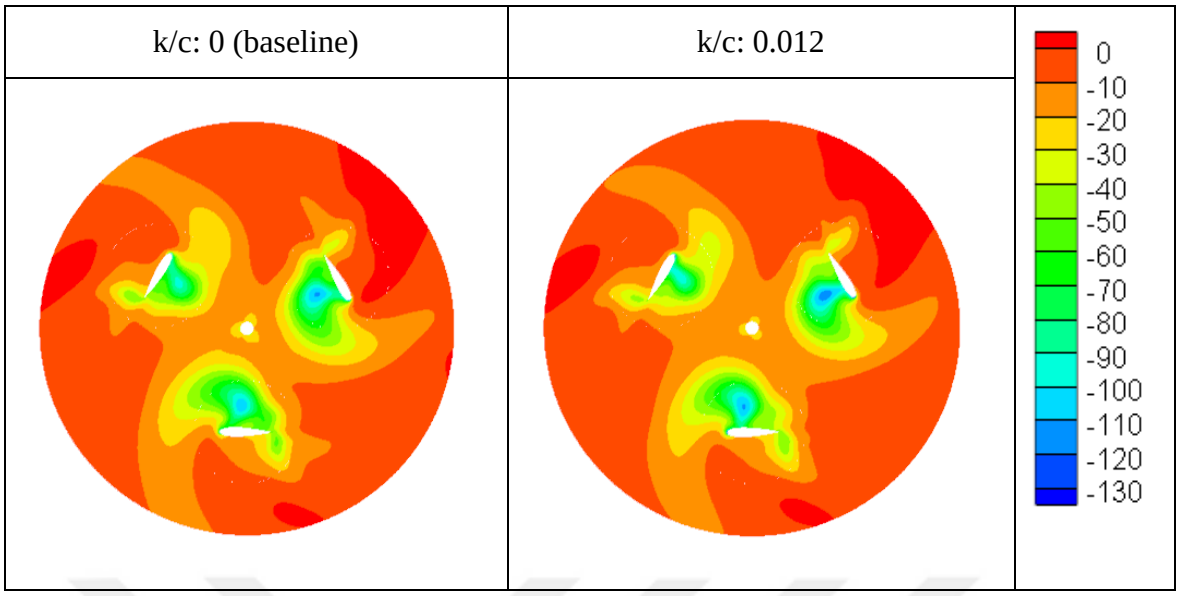

Figure 5.12. The mean pressure contour of the rotating region for baseline and k/c=0.012 between x/c=0 and x/c=0.50 at TSR = 0.75

The mean pressure distribution in the rotating region for both uncontrolled VAWT and controlled VAWT with the highest efficiency is given in Figure 5.12. The lift force is produced as a consequence of a pressure difference between two surfaces of a blade in both cases. Bernoulli's result, which accounts for the pressure difference between two surfaces of a blade, causes the flow pressure to decline where the flow velocity rises. The blade surface confronting the shaft (also defined as the suction surface) has relatively low pressure and thus ensures lift generation. Nevertheless, as the turbine rotates, the flow becomes comparatively complicated depending on the position of the blades. For both cases, it is seen that leading edge vortices formed by the effect of adverse pressure gradients in this region dominate. The modification of roughness elements to the leading edge of VAWT blades caused an increase in the negative pressure area. The increment in the power coefficient of the VAWT with roughness elements is, in particular, owing to this enhancement in the negative pressure coefficient.

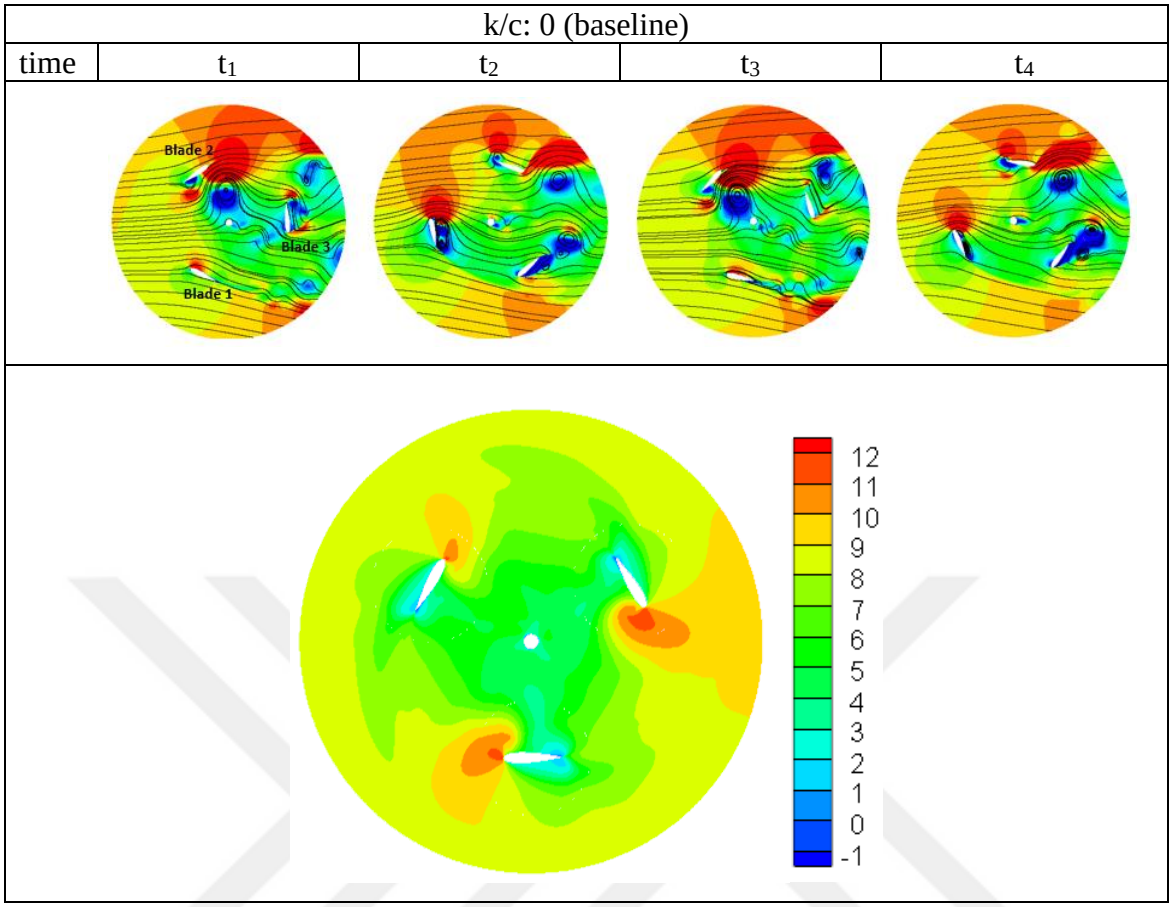

Figure 5.13. The x-velocity contours and streamlines of the rotating region over time and mean velocity contour for k/c: 0 (baseline)

Figure 5.13 and Figure 5.14 illustrate the x - velocity contours and flow streamline over time for the uncontrolled VAWT and the controlled VAWT with k/c: 0.012, respectively. In addition, the mean velocity contours were depicted in Figures 5.13 and 5.14 for both cases. When considering blade 1 for k/c: 0 and k/c: 0.012 cases, the increase in azimuthal angle results in flow separation and recirculation over time (from t_1 to t_4). The vortex pair formed on blade 1 at the t_2 and they merged at the t_3 developing a larger vortex. This vortex, moving away from this self-generating blade with the flow at t_4, continued to affect the flow structure in the rotating region.

Over the surface of blade 2 for k/c: 0 and k/c: 0.012 cases at t_1, trailing edge separation and large vortex formations between shaft and blade are observed. At t_4, boundary layer separation became more dominant, and the vortex pair evolved in the behind of wake region of blade 2. The region where the velocity is lower around blade 3 expands and its effect increases when the blade moves from the time of t_1 to t_2, leaving expanding vortexes behind the blade. At t_3 these vortexes are damped, and recirculating regions were observed at both the leading and trailing edges at t_4.

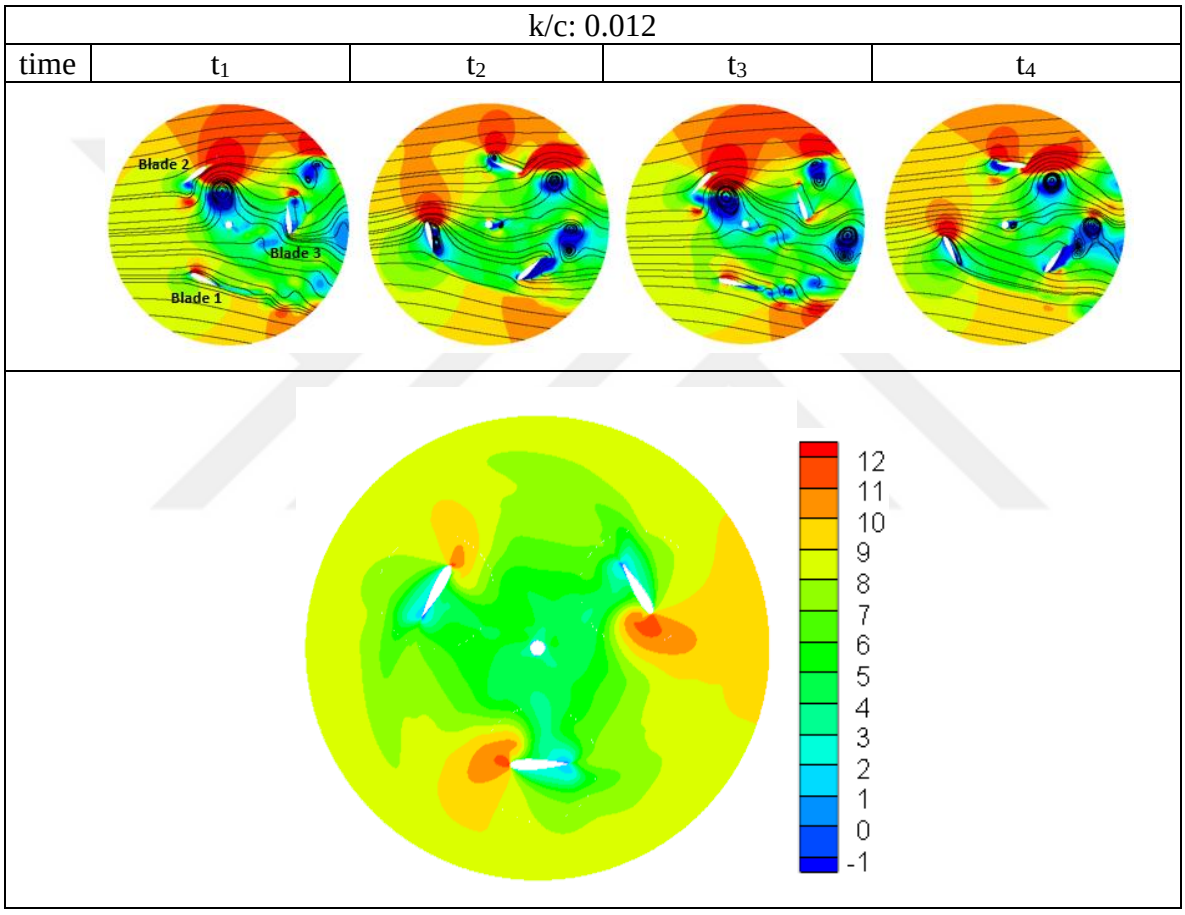

Figure 5.14. The x-velocity contours and streamlines of the rotating region over time and mean velocity contour for k/c: 0.012

The mean velocity topology for both baseline and controlled VAWT has not shown a substantial difference due to the dynamic conditions in the rotating region. However, flow separations on blade 1 at t_2 and blade 3 at t_4, which have similar azimuthal position, were reduced in the modified blade compared to the uncontrolled blade. The reduction in flow separation is achieved by applying the roughness element and showed more pronounced results in these positions (for blade 1 at t_2 and for blade 3 at t_4) of the blades. It can be

considered that the LSB has been relatively suppressed as the separating flow gains more momentum at these positions.

6. CONCLUSION AND FUTURE WORK

In this study, the numerical simulation of VAWT obtained from Transition SST model was investigated. As a result of the numerical analysis performed at different TSRs, the power coefficient obtained numerically at TSR=0.75 showed the best agreement with the experimental studies with a Cp value of 0.080. The low TSR numerical value (0.75) considered in this study was consistent with the experimental data, and it is validated.

Different roughness ratios and different positions over the blade were analyzed. In the first stage, the roughness was tested in small partial areas close to the leading edge of the blade to trigger the transition to turbulence over the blade. Different small increases in the power coefficient were obtained, to a maximum of 3%. Since these increased rates are small, then an alternative option was tried to see what would happen if 50% of the chord length was covered with roughness in the region close to the leading edge of the blade, and an increase in the power coefficient up to 46% was obtained, and it was seen that the aerodynamic performance of VAWTs increased with the use of roughness in a large area.

In VAWT, the power is produced from the lower blade and the AoA of the lower blade is important. The changing of the AoA of the lower blade produced the energy output until the blade stalled. After the blade stall, until the following blade produced the power, the C_p was decreased owing to the flow separations. Furthermore, the small length of roughness application over the blade surface did not affect the flow over the blades, and there is not an important increase in the C_p of these cases.

The numerical results of VAWT with roughness for different k/c ratios such as 0.003, 0.006, 0.009 and 0.012 between x/c=0 and x/c=0.50 was considered. The length of roughness application over the blade surface was raised, and aerodynamic performance was increased. As the length of roughness application over the blade surface increased, the time-dependent c_p increased. While the pre-stall and then the stall phenomena were seen in the C_p graph of the baseline blade, the stall was observed directly in the power coefficient graph of VAWT with roughness between x/c=0 and x/c=0.50.

To experimentally examine the effect of the roughness element on the flow characteristics of the turbine in the wake region, a hot-wire experiment can be performed in the different wake regions for a VAWT with uncontrolled and modified (with roughness element) blades. In addition, the performance can be examined by voltage measurements of VAWTs consisting of blades with and without roughness with the tachometer. The VAWT with modified blades can be analyzed at a wide range of TSR values.

REFERENCES

1. Zamani, M., Nazari, S., Moshizi, S. A., & Maghrebi, M. J. (2016). Three-dimensional simulation of J-shaped Darrieus vertical axis wind turbine. *Energy, 116*, 1243-1255.

2. Balduzzi, F., Bianchini, A., Carnevale, E. A., Ferrari, L., & Magnani, S. (2012). Feasibility analysis of a Darrieus vertical-axis wind turbine installation in the rooftop of a building. *Applied energy, 97*, 921-929.

3. Fiedler, A. J., & Tullis, S. (2009). Blade offset and pitch effects on a high solidity vertical axis wind turbine. *Wind engineering, 33*(3), 237-246.

4. Zhang, B., Song, B., Mao, Z., & Tian, W. (2017). A novel wake energy reuse method to optimize the layout for Savonius-type vertical axis wind turbines. *Energy, 121*, 341-355.

5. Rolin, V. F., & Porté-Agel, F. (2018). Experimental investigation of vertical-axis wind-turbine wakes in boundary layer flow. *Renewable energy, 118*, 1-13.

6. Möllerström, E., Ottermo, F., Goude, A., Eriksson, S., Hylander, J., & Bernhoff, H. (2016). Turbulence influence on wind energy extraction for a medium size vertical axis wind turbine. *Wind Energy, 19(11)*, 1963-1973.

7. Anagnostopoulou, C., Kagemoto, H., Sao, K., & Mizuno, A. (2016). Concept design and dynamic analyses of a floating vertical-axis wind turbine: case study of power supply to offshore Greek islands. *Journal of Ocean Engineering and Marine Energy, 2*, 85-104. to offshore Greek islands. J. Ocean Eng. Marine Energy, 2, 85-104.

8. Rezaeiha, A., Kalkman, I., & Blocken, B. (2017). Effect of pitch angle on power performance and aerodynamics of a vertical axis wind turbine. *Applied energy, 197*, 132-150.

9. Subramanian, A., Yogesh, S. A., Sivanandan, H., Giri, A., Vasudevan, M., Mugundhan, V., & Velamati, R. K. (2017). Effect of airfoil and solidity on performance of small scale vertical axis wind turbine using three dimensional CFD model. *Energy, 133*, 179-190.

10. Bachant, P., & Wosnik, M. (2016). Effects of Reynolds number on the energy conversion and near-wake dynamics of a high solidity vertical-axis cross-flow turbine. *Energies, 9(2)*, 73.

11. Wang, Z., & Zhuang, M. (2017). Leading-edge serrations for performance improvement on a vertical-axis wind turbine at low tip-speed-ratios. *Applied Energy, 208*, 1184-1197.

12. Wang, Q., Chen, J., Pang, X., Li, S., & Guo, X. (2013). A new direct design method for the medium thickness wind turbine airfoil. *Journal of Fluids and Structures, 43*, 287-301.

13. Jin, X., Zhao, G., Gao, K., & Ju, W. (2015). Darrieus vertical axis wind turbine: Basic research methods. *Renewable and Sustainable Energy Reviews, 42*, 212-225.

14. Li, X., Yang, K., Bai, J., & Xu, J. (2016). A new optimization approach to improve the overall performance of thick wind turbine airfoils. *Energy, 116*, 202-213.

15. Lei, H., Zhou, D., Lu, J., Chen, C., Han, Z., & Bao, Y. (2017). The impact of pitch motion of a platform on the aerodynamic performance of a floating vertical axis wind turbine. *Energy, 119*, 369-383.

16. Ribeiro, A. F. P., Awruch, A. M., & Gomes, H. M. (2012). An airfoil optimization technique for wind turbines. *Applied Mathematical Modelling, 36*(10), 4898-4907.

17. Balduzzi, F., Drofelnik, J., Bianchini, A., Ferrara, G., Ferrari, L., & Campobasso, M. S. (2017). Darrieus wind turbine blade unsteady aerodynamics: a three-dimensional Navier-Stokes CFD assessment. *Energy, 128*, 550-563.

18. Ferreira, C. S., & Geurts, B. (2015). Aerofoil optimization for vertical-axis wind turbines. *Wind Energy, 18*(8), 1371-1385.

19. Miao, W., Liu, Q., Zhang, Q., Xu, Z., Li, C., Yue, M., ... & Ye, Z. (2023). Recommendation for strut designs of vertical axis wind turbines: Effects of strut profiles and connecting configurations on the aerodynamic performance. *Energy Conversion and Management, 276*, 116436.

20. Abbasi, R., Ketabdari, M.J. (2022) Enhancement of OWC Wells turbine efficiency and performance using riblets covered blades, a numerical study. *Energy Conversion and Management, 254*, 115212.

21. Manolesos, M., Chng, L., Kaufmann, N., Ouro, P., Ntouras, D., & Papadakis, G. (2023). Using vortex generators for flow separation control on tidal turbine profiles and blades. *Renewable Energy, 205*, 1025-1039.

22. Özden, M., Genç, M. S., & Koca, K. (2023). Investigation of the effect of hidden vortex generator-flap integrated mechanism revealed in low velocities on wind turbine blade flow. *Energy Conversion and Management*, 287, 117107.

23. Genç, M. S., Açıkel, H. H., & Koca, K. (2020). Effect of partial flexibility over both upper and lower surfaces to flow over wind turbine airfoil. *Energy Conversion and Management, 219*, 113042.

24. Koca, K., Genç, M. S., Bayır, E., & Soğuksu, F. K. (2022). Experimental study of the wind turbine airfoil with the local flexibility at different locations for more energy output. *Energy, 239*, 121887.

25. Koca, K., Genç, M. S., & Ertürk, S. (2022). Impact of local flexible membrane on power efficiency stability at wind turbine blade. *Renewable Energy, 197*, 1163-1173.

26. Stuart, J. G., Wright, A. D., & Butterfield, C. P. (1996). *Considerations for an integrated wind turbine controls capability at the National Wind Technology Center: an aileron control case study for power regulation and load mitigation* (No. NREL/TP-440-21335; CONF-960630-2). National Renewable Energy Lab.(NREL), Golden, CO (United States).

27. Horcas, S. G., Madsen, M. H. A., Sørensen, N. N., Zahle, F., & Barlas, T. (2022). Influence of the installation of a trailing edge flap on the vortex induced vibrations of a wind turbine blade. *Journal of Wind Engineering and Industrial Aerodynamics*, 229, 105118.

28. Zhu, H., Hao, W., Li, C., Ding, Q., & Wu, B. (2019). Application of flow control strategy of blowing, synthetic and plasma jet actuators in vertical axis wind turbines. *Aerospace Science and Technology*, *88*, 468-480.

29. Greenblatt, D., Ben-Harav, A., & Mueller-Vahl, H. (2014). Dynamic stall control on a vertical-axis wind turbine using plasma actuators. *AIAA journal*, *52*(2), 456-462.

30. Greenblatt, D., Schulman, M., & Ben-Harav, A. (2012). Vertical axis wind turbine performance enhancement using plasma actuators. *Renewable Energy*, *37*(1), 345-354.

31. Chen, L., Yang, Y., Gao, Y., Gao, Z., Guo, Y., & Sun, L. (2019). A novel real-time feedback pitch angle control system for vertical-axis wind turbines. *Journal of Wind Engineering and Industrial Aerodynamics*, *195*, 104023.

32. Miao, W., Liu, Q., Xu, Z., Yue, M., Li, C., & Zhang, W. (2022). A comprehensive analysis of blade tip for vertical axis wind turbine: Aerodynamics and the tip loss effect. *Energy Conversion and Management*, *253*, 115140.

33. Ma, N., Lei, H., Han, Z., Zhou, D., Bao, Y., Zhang, K., ... & Chen, C. (2018). Airfoil optimization to improve power performance of a high-solidity vertical axis wind turbine at a moderate tip speed ratio. *Energy*, *150*, 236-252.

34. Elkhoury, M., Kiwata, T., & Aoun, E. (2015). Experimental and numerical investigation of a three-dimensional vertical-axis wind turbine with variable-pitch. *Journal of wind engineering and Industrial aerodynamics*, *139*, 111-123.

35. Tescione, G., Ragni, D., He, C., Ferreira, C. S., & Van Bussel, G. J. W. (2014). Near wake flow analysis of a vertical axis wind turbine by stereoscopic particle image velocimetry. *Renewable Energy*, *70*, 47-61.

36. Vergaerde, A., De Troyer, T., Muggiasca, S., Bayati, I., Belloli, M., Kluczewska-Bordier, J., ... & Runacres, M. C. (2020). Experimental characterisation of the wake behind paired vertical-axis wind turbines. *Journal of Wind Engineering and Industrial Aerodynamics*, *206*, 104353.

37. Santamaría, L., Oro, J. M. F., Díaz, K. M. A., Meana-Fernández, A., Pereiras, B., & Velarde-Suárez, S. (2022). Novel methodology for performance characterization of vertical axis wind turbines (VAWT) prototypes through active driving mode. *Energy Conversion and Management*, *258*, 115530.

38. Subramanian, A., Yogesh, S. A., Sivanandan, H., Giri, A., Vasudevan, M., Mugundhan, V., & Velamati, R. K. (2017). Effect of airfoil and solidity on performance of small scale vertical axis wind turbine using three dimensional CFD model. *Energy*, *133*, 179-190.

39. Miller, M. A., Duvvuri, S., & Hultmark, M. (2021). Solidity effects on the performance of vertical-axis wind turbines. *Flow*, *1*, E9.

40. Castelli, M. R., Englaro, A., & Benini, E. (2011). The Darrieus wind turbine: Proposal for a new performance prediction model based on CFD. *Energy, 36*(8), 4919-4934.

41. Howell, R., Qin, N., Edwards, J., & Durrani, N. (2010). Wind tunnel and numerical study of a small vertical axis wind turbine. *Renewable energy, 35*(2), 412-422.

42. Li, C., Zhu, S., Xu, Y. L., & Xiao, Y. (2013). 2.5 D large eddy simulation of vertical axis wind turbine in consideration of high angle of attack flow. *Renewable energy, 51*, 317-330.

43. Rezaeiha, A., Montazeri, H., & Blocken, B. (2019). On the accuracy of turbulence models for CFD simulations of vertical axis wind turbines. *Energy, 180*, 838-857.

44. Elsakka, M. M., Ingham, D. B., Ma, L., & Pourkashanian, M. (2019). CFD analysis of the angle of attack for a vertical axis wind turbine blade. *Energy Conversion and Management, 182*, 154-165.

45. Taylor, H. D. (1947). The elimination of diffuser separation by vortex generators. *Research department report no. r-4012-3, United Aircraft Corporation, East Hartford, Connecticut*, 103.

46. Gao, L., Zhang, H., Liu, Y., & Han, S. (2015). Effects of vortex generators on a blunt trailing-edge airfoil for wind turbines. *Renewable Energy, 76*, 303-311.

47. Özden, M., Genç, M. S., & Koca, K. (2023). Investigation of the effect of hidden vortex generator-flap integrated mechanism revealed in low velocities on wind turbine blade flow. *Energy Conversion and Management, 287*, 117107.

48. Weick, F. E., & Shortal, J. A. (1933*). The effect of multiple fixed slots and a trailing-edge flap on the lift and drag of a Clark Y airfoil* (No. NACA-TR-427).

49. Axelson, J. A. (1954). *Investigation of a slat in several different positions on an NACA 64A010 airfoil for a wide range of subsonic Mach numbers* (No. 3129). National Advisory Committee for Aeronautics.

50. Genç, M. S., Kaynak, Ü., & Lock, G. D. (2009). Flow over an aerofoil without and with a leading-edge slat at a transitional Reynolds number. *Proceedings of the Institution of Mechanical Engineers, Part G: Journal of Aerospace Engineering, 223*(3), 217-231.

51. Fish, F., & Lauder, G. V. (2006). Passive and active flow control by swimming fishes and mammals. *Annu. Rev. Fluid Mech., 38*, 193-224.

52. Ibrahim, I. H., & New, T. H. (2015, June). Tubercle modifications in marine propeller blades. In *10th Pacific Symposium on Flow Visualization and Image Processing* (pp. 1-11). Naples Italy.

53. Ismail, M. F., & Vijayaraghavan, K. (2015). The effects of aerofoil profile modification on a vertical axis wind turbine performance. *Energy*, 80, 20-31.

54. Genc, M. S., Koca, K., Acikel, H. H. (2019). Investigation of pre-stall flow control on wind turbine blade airfoil using roughness element. *Energy*, 176, 320-334.

55. Koca, K., Genç, M. S., & Açikel, H. H. (2016, May). Roughness effect on flow over wind turbine airfoil. In *The International Symposium on Sustainable Aviation (ISSA-2016)* (Vol. 29).

56. Koca, K., Genç, M.S., Açikel, H.H. Experimental Investigation of Surface Roughness Effect over Wind Turbine Airfoil. (2016), *Çukurova Üniversitesi Mühendislik-Mimarlık Fakültesi Dergisi, cilt.31,* 127-133.

57. Koca, K. (2016). *The flow control with roughness devices over wind turbine airfoil* (Doctoral dissertation, MSc. Thesis 2016 Graduate School of Natural and Applied Sciences. Turkey: Erciyes University, Kayseri).

58. Puckert, D. K., & Rist, U. (2018). Experiments on critical Reynolds number and global instability in roughness-induced laminar–turbulent transition. *Journal of Fluid Mechanics*, *844*, 878-904.

59. Pires, O., Munduate, X., Boorsma, K., Yilmaz, O. C., Madsen, H. A., & Timmer, W. A. (2018, June). Experimental investigation of surface roughness effects and transition on wind turbine performance. In *Journal of Physics: Conference Series* (Vol. 1037, No. 5, p. 052018). IOP Publishing.

60. Zhang, Y., Xu, J., Li, Y., Qiao, L., & Bai, J. (2022). Modeling of surface roughness effects on bypass and laminar separation bubble-induced transition for turbomachinery flows. *Physics of Fluids*, *34*(4), 044108.

61. Rogowski, K. (2019). CFD Computation of the H-Darrieus wind turbine—The impact of the rotating shaft on the rotor performance. *Energies*, *12*(13), 2506.

62. Ogrodnik, N., Sudasinghe, A., Heiber, E., abo el Ella, H., Fereidooni, A., Matida, E., & Kaya, T. (2023). Pseudo three-dimensional numerical investigation of legacy vertical axis wind turbine configurations. Energy Conversion and Management: X, 17, 100338.

63. Shyy, W., Lian, Y., Tang, J., Viieru, D., & Liu, H. (2008). *Aerodynamics of low Reynolds number flyers.*

64. Horton, H. P. (1968). *Laminar separation bubbles in two and three dimensional incompressible flow* (Doctoral dissertation, Queen Mary University of London).

65. Wynnychuk, D. W., & Yarusevych, S. (2020). Characterization of laminar separation bubbles using infrared thermography. *AIAA Journal*, 58(7), 2831-2843.

66. Choudhry, A., Arjomandi, M., & Kelso, R. (2015). A study of long separation bubble on thick airfoils and its consequent effects. *International Journal of Heat and Fluid Flow*, 52, 84-96.

67. Genç, M. S., Karasu, İ., & Açıkel, H. H. (2012). An experimental study on aerodynamics of NACA2415 aerofoil at low Re numbers. *Experimental Thermal and Fluid Science*, *39*, 252-264.

68. Clausen, P. D., & Wood, D. H. (1999). Research and development issues for small wind turbines. *Renewable Energy*, *16*(1-4), 922-927.

69. Samson, A., & Sarkar, S. (2016). An experimental investigation of a laminar separation bubble on the leading-edge of a modelled aerofoil for different Reynolds numbers. *Proceedings of the Institution of Mechanical Engineers, Part C: Journal of Mechanical Engineering Science, 230*(13), 2208-2224.

70. Ketz, J., & Plotkin, A. (1991). *Low-speed aerodynamics: from wing theory to panel methods*. McGraw-Hill, Incorporated.

71. Suzen, Y., & Huang, P. (2000, January). An intermittency transport equation for modeling flow transition. In *38th Aerospace Sciences Meeting and Exhibit* (p. 287).

72. Menter, F. (1993, July). Zonal two equation kw turbulence models for aerodynamic flows. In *23rd fluid dynamics, plasmadynamics, and lasers conference* (p. 2906).

73. Stripf, M., Schulz, A., & Wittig, S. (2005). Surface roughness effects on external heat transfer of a HP turbine vane. *J. Turbomach., 127*(1), 200-208.

74. Langtry, R., & Menter, F. (2006). Overview of industrial transition modelling in CFX. *ANSYS Germany GmbH, ANSYS CFX*.

75. Blades, E. L., & Marcum, D. L. (2007). A sliding interface method for unsteady unstructured flow simulations. *International Journal for Numerical Methods in Fluids, 53*(3), 507-529.

Gazili olmak ayrıcalıktır